



Experimental wind tunnel dataset of wake and turbine measurements for wind farm control

Filippo Campagnolo, Doruk Aktan, Davide Bortolin, Simone Tamaro, Franz V. Mühle, and Carlo L. Bottasso

Wind Energy Institute, Technische Universität München, Garching bei München, D-85748 Germany

Correspondence: Carlo L. Bottasso (carlo.bottasso@tum.de)

Abstract. Open-access experimental datasets play a central role in validating and benchmarking numerical models used in wind energy and wind-farm control research. However, publicly available datasets providing time-resolved turbine loads, actuator commands, and inflow characterisation under controlled operation remain scarce.

This paper presents a new open-access experimental dataset from wind-tunnel experiments featuring actuated, instrumented, scaled wind turbine models. The database includes time-resolved measurements of tower-base and rotating-shaft moments, rotor speed, generated torque and power, blade pitch angles, nacelle yaw angle, and controller commands. The inflow conditions are described in terms of wind speed, wind direction, air density, and wake-flow measurements, enabling detailed analyses of turbine response and controller behaviour under consistent, repeatable conditions.

The experiments cover a wide range of wake-control strategies, including yaw-based wake steering, curtailment and derating, Helix control, dynamic yaw actuation, Pulse wake mixing, individual pitch control, and several combinations of these strategies. The simultaneous availability of actuator commands, measured turbine response, and time-resolved structural loads enables detailed investigation of the controller performance, load variability, and dynamic turbine behaviour induced by active wake-control strategies.

In addition to the experimental measurements, the dataset is complemented by numerical models of the experiments, providing a reproducible experimental-numerical benchmarking framework that enables dataset extension, sensitivity analyses, and systematic validation of control-oriented aeroelastic and wake-interaction models.

The dataset is intended to support the validation and benchmarking of numerical tools for wind-farm control, the assessment of fatigue-relevant loading under wake-control operations, and to strengthen community efforts to improve transparency, reproducibility, and model fidelity in wind-farm design and control research.

20 1 Introduction

Open-access experimental datasets have become a cornerstone for validation, benchmarking, and reproducibility across multiple engineering disciplines, including aeronautics, rotorcraft dynamics, and wind engineering.

In aeronautics, reference geometries and wind tunnel data – such as those of the NASA Common Research Model (Rivers and Dittberner, 2014) – have supported large-scale community benchmarking initiatives to assess the predictive capabilities



25 of Computational Fluid Dynamics (CFD) solvers and uncertainty quantification strategies. Coordinated efforts such as the
AIAA Drag Prediction Workshops (Levy et al., 2002; Lafin et al., 2004; Levy et al., 2013; Tinoco et al., 2018; Tinoco,
2023) have demonstrated that shared experimental baselines can accelerate advances in turbulence modelling, mesh generation
practices, and aerodynamic prediction accuracy. Comparable progress has been achieved within the rotorcraft community,
where comprehensive experimental campaigns such as HART II (van der Wall et al., 2004) have made subsets of time-resolved
30 aerodynamic and structural measurements publicly available. These datasets, often complemented by structured validation
workshops (van der Wall, 2011; Smith et al., 2013), have contributed significantly to improvements in the modelling of unsteady
aerodynamics, aeroelastic coupling, and prediction of dynamic loads.

In wind engineering, open-access datasets derived from both laboratory and full-scale measurements have long served to
bridge the gap between controlled wind-tunnel conditions and the complexity of real atmospheric inflows. Publicly available
35 measurements of wind-induced pressures, structural loads, and flow statistics, like the ones reported in Tominaga and Shirzadi
(2021); Styrk Andersen et al. (2022); Shaukat and Giljarhus (2024); Ishihara and Zhou (2025), have enabled detailed vali-
dation of numerical models, extending from mean quantities to spectral characteristics, intermittency, and extreme response
events. These efforts have underscored the critical importance of time-resolved datasets for characterising flow-structure in-
teraction under turbulent inflow and for enhancing the reliability of predictive tools used in structural design and performance
40 assessment (Kareem, 2010; Holmes, 2015).

The wind energy sector has particularly benefited from coordinated experimental and numerical benchmarking efforts.
Laboratory-scale campaigns such as the Unsteady Aerodynamics Experiment (UAE Phase VI) (Hand et al., 2001), the MEX-
ICO (Snel et al., 2007; Schepers et al., 2012, 2014), and New MEXICO (Boorsma and Schepers, 2014, 2016) projects have
provided high-quality aerodynamic and load measurements for the validation of blade-resolved CFD and aeroelastic models.
45 At full scale, coordinated measurement programs such as DanAero (Madsen et al., 2010) have offered valuable insight into
turbine response under realistic inflow and wake conditions. In parallel, open numerical datasets and reference models released
within the IEA Wind Task 37 (Bortolotti et al., 2019) have established common baselines for reproducible simulations and
tool-to-tool comparison.

Despite these advances, open-access datasets specifically tailored to wind-farm control and wake-interaction studies remain
50 scarce (Veers et al., 2023). Existing experimental investigations of wake steering and active wake control often focus on
aggregated power performance metrics (Doekemeijer et al., 2021; Fleming et al., 2019, 2020), and time-resolved measurements
– particularly for field-scale experiments – are seldom publicly released. A case in point is the recent ambitious AWAKEN
experiment (Moriarty et al., 2020), an effort of unprecedented scope and breadth that has collected extensive measurements,
of which only a small fraction has ever been released to the scientific community. Moreover, available datasets – e.g., Sengers
55 et al. (2023); Fontanella et al. (2025) – typically emphasize wake or flow-field characterization, while detailed on-board turbine
measurements under active wake-control operation are much less common, if at all available outside of small closed consortia.
This lack of high-resolution actuator and load data limits the validation of control-oriented load models. It also hinders the
assessment of load variability arising from wake-mixing strategies.



The dataset presented in this work addresses this gap by providing a new open-access experimental database specifically
60 designed for wind-farm control and wake-interaction studies. The dataset was obtained from wind-tunnel experiments featur-
ing small clusters of scaled, sensorized, and actuated wind turbines of the G1 type (Bottasso and Campagnolo, 2022). The
measurements include time-resolved tower-base moments, rotating-shaft moments, rotor speed, generated torque and power,
commanded and measured blade pitch for each blade, and nacelle yaw angle. Inflow conditions are characterized by wind
speed, wind direction, air density, and wake-flow measurements, enabling comprehensive analyses of both turbine response
65 and controller behaviour under known, repeatable conditions.

The experiments cover a broad range of wake-control strategies, including yaw-based wake steering, curtailment and de-
rating strategies, Helix control (Frederik et al., 2020a), dynamic yaw actuation, Pulse-based wake mixing (Frederik et al.,
2020b, 2025), individual pitch control (IPC) for load reduction, and several combined strategies. By combining actuator
commands, measured responses, and time-resolved structural loads, the dataset supports a detailed evaluation of controller
70 performance, load variability, and the dynamic turbine behaviour induced by active wake control.

This dataset is expected to support several research efforts: validation of control-oriented aeroelastic and wake-interaction
models, assessment of load variability and fatigue-relevant statistics under wake-control operation, and benchmarking of nu-
merical tools used for wind-farm control synthesis. More broadly, it contributes to ongoing community efforts to enhance
transparency, reproducibility, and model fidelity in wind-farm control research.

75 Alongside the experimental measurements, the database provides numerical models designed to replicate the experimental
setups. This combined experimental-numerical framework transforms the dataset into a reproducible benchmarking platform,
enabling the extension of the database beyond the measured conditions and facilitating systematic investigations of modelling
assumptions and parameter sensitivity.

This paper is organised as follows. Section 2 presents the experimental setup. Section 3 discusses the execution of the
80 experiments, the data post-processing, and the expected measurement uncertainty. The experimental dataset is described in
Sect. 4, while the numerical models are presented in Sect. 5, followed by the conclusions in Sect. 6.

2 Experimental setup

2.1 Wind tunnel

All tests were conducted in the boundary layer test section of the wind tunnel at the Politecnico di Milano (POLIMI), which
85 consists of a closed-loop vertical conduit (Diana et al., 1998). The section, shown in Fig. 1a, is located in the return line of the
facility and extends longitudinally for 35.6 m, with a width of 13.84 m and a height of 3.84 m. The test chamber is equipped
with a 13 m diameter rotating table, whose center is located along the centerline, at a distance of 29.1 m from the inlet. The
rotation of the table Φ , defined as positive if clockwise when viewed from above, allows simulating the effect of wind direction
on the performance of the experimental setup. Φ is zero when the centerline of the turntable is aligned with the centerline of
90 the test section, as shown in Fig. 1b. Rotation is achieved by a driving tyred wheel that engages with the outer perimeter of the
turntable, using the position measured by an absolute rotary encoder with 8192 Pulses Per Revolution (PPR) as feedback. A



limitation on the maximum acceleration is enforced to prevent the tyre from slipping (Campagnolo et al., 2020b). The turntable rotation is measured and converted into an analog signal for acquisition by an external system.

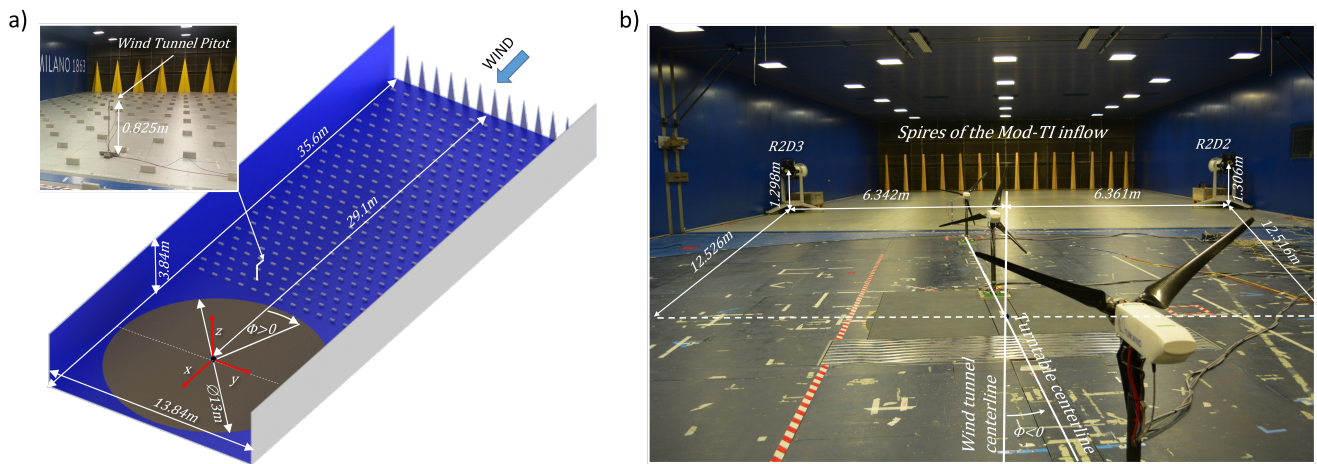


Figure 1. Main dimensions of the test section of the POLIMI wind tunnel, including the distance of the turntable center from the inlet (a). Boundary layer test section equipped with the spires used to simulate the Mod-TI inflow (b). Wind turbine and flow-measurement device positions are measured relative to the depicted reference frame, whose origin lies at the turntable center.

2.1.1 Boundary layer simulation

95 Given the relatively modest length of the test chamber compared to the dimensions of its cross-section, a proper simulation of the atmospheric boundary layer requires the installation of obstacles both at the inlet (spires, triangular or trapezoidal in shape) and on the floor (rectangular bricks) (Cermak, 2003). The size and precise position of these obstacles depend on the desired characteristics of the boundary layer, and particularly on the velocity and turbulence profiles. The dataset described in this article was obtained by reproducing four different inflows in the test section:

- 100 – Low-TI: obtained with an empty test section; it is characterized by a low turbulence inflow of approximately 1-2% (Diana et al., 1998).
- Mod-TI: obtained by installing 14 trapezoidal spires of type A (lower base width 0.26 m, top width 0.1 m, height 2 m) at the inlet, spaced 1 m apart, as shown in Fig. 1b; it has a turbulence of about 6% at the apex of the G1 rotor.
- High-TI: obtained by installing 9 type B triangular spires (base 0.8 m, height 2.5 m) at the inlet, spaced 1.55 m apart, as shown in Fig. 2a. Rectangular bricks (height 0.1 m, width 0.2 m, depth 0.06 m) are aligned diagonally on the floor, with a longitudinal and lateral spacing of 1.1 m. It has a turbulence of about 13.5% at the apex of the G1 rotor.



110

115

- Extreme-TI: obtained by installing 9 type *B* triangular spires at the inlet, spaced 1.55 m apart and interspersed with 8 type *A* trapezoidal spires. In addition, five different types of bricks are disposed on the floor, as shown in Fig. 2b: one row of bricks of type *A* (height 0.74 m, width 0.39 m, depth 0.15 m) placed immediately downstream of the spires and aligned with the spires of type *A*; one row of bricks of type *B* (height 0.5 m, width 0.4 m, depth 0.15 m) placed next, aligned with the spires of type *B*; one row of bricks of type *C* (height 0.3 m, width 0.24 m, depth 0.24 m) placed next, followed by a row of bricks of type *D* (height 0.24 m, width 0.22 m, depth 0.11 m), and several rows of bricks of type *E* (height 0.2 m, width 0.2 m, depth 0.06 m) up to the turntable. The bricks of types *C*, *D*, and *E* are placed diagonally on the floor at a longitudinal and lateral distance of 0.9 m. The generated inflow has a turbulence of approximately 22% at the apex of the G1 rotor.

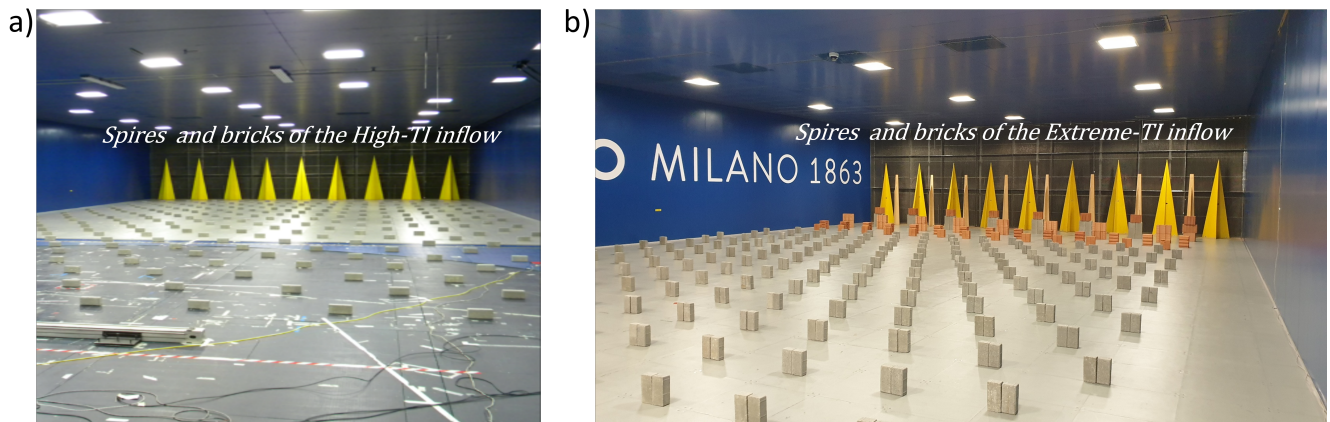


Figure 2. Spires and bricks used to simulate the High-TI boundary layer (a). Spires and bricks used to simulate the Extreme-TI boundary layer (b).

2.1.2 Wind tunnel sensors

The wind tunnel is equipped with sensors that measure the thermohygrometric parameters of the air in the boundary-layer test section. Specifically, atmospheric pressure is measured by an *Effa AK-S 900-1060* transducer (uncertainty ± 0.5 hPa), temperature by a *Meson TH 12-U* thermocouple transducer (uncertainty $\pm 0.1\%$ of Full Scale), and relative humidity (RH) with a *Rense 741* transducer (uncertainty $\pm 2\%$ RH). These measurements are used to estimate the air density ρ as explained in Davis (1992).

The test section is equipped with Pitot tubes at the inlet and on the ceiling. The measurements from these sensors can be useful for controlling the wind tunnel fans, but they do not provide an accurate velocity measurement upstream of the turbine cluster being tested. For this reason, an additional Pitot tube is placed in front of the cluster, at hub height. The dynamic pressure p_{dyn} of the Pitot tube is measured by an *MKS Baratron-Type 226A* pressure transducer, characterized by an accuracy



$\Delta p_{\text{dyn}} = \pm 0.4$ Pa, and can also be acquired by external data acquisition systems. The freestream velocity representative of the undisturbed flow is then obtained as $u_{\infty} = \sqrt{2p_{\text{dyn}}/\rho}$.

2.2 Scaled wind turbine model

The wind turbine model used in the experiments, shown in Fig. 3, features a rotor diameter D of 1.1 m and a hub height z_H of 130 0.825 m. Its rated power P_R , torque Q_R , and rotor speed Ω_R are 46 W, 0.517 Nm, and 850 rpm, respectively. The cut-in and cut-out velocities are 2 ms^{-1} and 9 ms^{-1} , respectively, while the rated wind speed is around 5.8 ms^{-1} . The time compression ratio is equal to 80, i.e. time flows in the experiments 80 times faster than at full scale (Bottasso and Campagnolo, 2022). The rotor axis is parallel to the ground. The rotor is upwind, not coned, and rotates clockwise if viewed from upstream. The rotor has an overhang of 0.123 m from the tower axis. A 12-channel slip ring is used to transmit power, measurement, and 135 control signals between the rotor and the fixed frame. The machine design process is extensively discussed in Bottasso and Campagnolo (2022). The following sections, instead, report a detailed description of the G1 hardware and software.

2.2.1 Actuators

The G1 is equipped with Maxon motors (Maxon Motor AG, 2026) that serve as pitch, yaw, and torque actuators. Each blade is individually controlled through a brushed motor *DCX16L GB SL 24V*, housed within the hollow root of the blade, equipped 140 with a planetary gear-head *GPX19 A* (nominal gear ratio 62:1) and a co-located relative encoder *ENX10 EASY* (128 PPR). An *EPOS2 24/2 DCX* positioning controller is used to actuate the motor position. The actuation system is preloaded using a torsion spring, as described in Campagnolo (2013). This solution removes gearbox backlash, enabling the encoder to accurately measure the blade pitch; additionally, it passively sets a high blade pitch in the event of controller malfunction or power loss. The maximum pitch rate is 400°s^{-1} , equivalent to 5°s^{-1} at full scale because of time compression. For each blade, the 145 actuator is homed using the output of a *Honeywell SS496A1* Hall-effect sensor mounted on the hub. The sensor measures the magnetic flux induced by a magnetic dipole made of two NdFeB *Supermagnete Q-05-1.5-01-N* magnets placed side by side. The magnets are positioned at the base of the blade and thus rotate with it. During the homing procedure, the blades are slowly rotated until the Hall sensor detects zero magnetic flux, which occurs when the sensor centerline is aligned with the magnetic dipole centerline; this triggers the encoder reset.

150 The torque generator consists of a brushless motor *EC-4pole22 BL Y 90W KL*, equipped with a planetary gear-head *GP22HP 2.4Nm 2ST KL* (nominal gear ratio 14:1) and a co-located tachometer *HEDL 5540* (500 PPR). An *ESCON 50/5* servo-controller is used to manage the current flowing through the motor windings.

The G1 can be equipped with two different yaw actuation systems: a standard and a fast one, shown in Fig. 3a and 3b, respectively.

155 The standard yaw actuator, located inside the hollow tower, consists of a brushed motor *DCX32L GB KL 24V* equipped with a planetary gear-head *GPX37 LZ* (nominal gear ratio 231:1). The nacelle position is measured by a non-co-located optical encoder *US-DIGITAL E6-10000-750-IE-D-H-D-3* (10000 PPR). An *EPOS2 24/2* positioning controller, used to actuate the

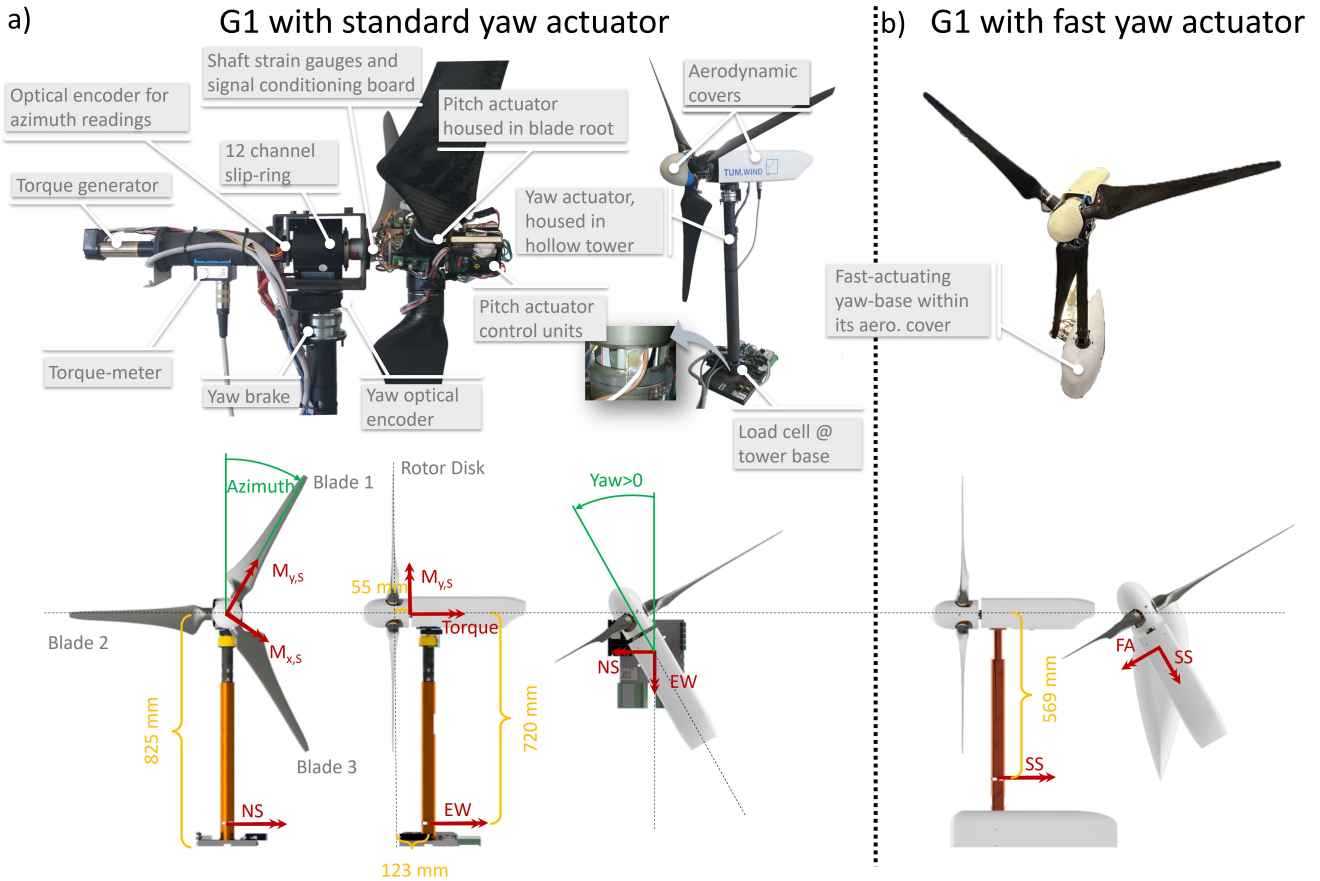


Figure 3. Top: overview of the G1 model and its main features (Bottasso and Campagnolo, 2022). Bottom: G1 sensed quantities and corresponding reference frames. G1 with standard yaw actuator (a); G1 with fast yaw actuator (b).

motor position, allows to rotate the entire rotor-nacelle assembly at a maximum yaw rate of 20°s^{-1} , equivalent to $0.25^{\circ}\text{s}^{-1}$ at full scale.

160 The fast yaw actuation is provided by a mechanism located at the base of the tower and concealed within an airfoil-shaped cover. The mechanism, described in detail in Mühle et al. (2022), consists of a *RE40* $\varnothing 40\text{ mm}$ brushed motor, a *Wittenstein TK+* right-angle gearbox (nominal gear ratio 100:1) characterized by a very small backlash ($\gamma_{\text{BL}} = 4$ arc minutes), and a co-located optical encoder *HEDS 5540* (500 PPR). An *EPOS2 24/5* positioning controller enables the entire rotor-nacelle assembly to rotate with a maximum yaw rate equivalent to 0.9°s^{-1} at full scale.



165 2.2.2 Sensors

Several physical quantities are measured in the reference systems shown in Fig. 3. The blades and their corresponding actuators are numbered according to the order in which they pass through the vertical axis during a rotation. The azimuth position ψ of the first blade is measured by an optical encoder *US-DIGITAL HUBDISK-2-2500-1000-IE* (2500 PPR). It is defined as the angle between the vertical axis and the pitch axis, measured clockwise when looking downstream, and it is null when the first blade points upward. The pitch β_i of the i -th blade is measured by the built-in encoder, and it is positive when the blade is pitched to feather. The rotation of the nacelle γ_{nac} is measured by the optical encoder of the yaw actuator. It is the angle between the rotor axis and the turntable centerline, positive for counter-clockwise rotation when viewed from above. The rotor speed Ω is sensed by the tachometer of the generator.

The G1 is equipped with several strain gauges arranged in full Wheatstone bridges. Two full bridges are placed close to the tower base, at a distance z_{SG} of 0.72 m or 0.569 m from the rotor axis for the standard and fast yaw actuator, respectively. For the standard yaw actuator, the strain gauges are located below the yaw system and are therefore fixed with respect to the turntable; their sensed bending moments are noted East-West (EW, aligned with the turntable centerline) and North-South (NS, forming a right-handed triad with EW and the yaw axis). For the fast yaw actuator, the strain gauges are placed above the yaw system and therefore rotate with respect to the turntable; their sensed moments are noted Side-Side (SS, aligned with the rotor axis) and Fore-Aft (FA, forming a right-handed triad with SS and the yaw axis).

Three full bridges are placed on the rotating shaft between the rotor and the front bearing, 0.055 m from the rotor apex. They measure the main shaft torque Q_S and two out-of-plane bending moments: the moment $M_{y,S}$, aligned with the pitch axis of the first blade, and the moment $M_{x,S}$, which forms a right-handed triad with the torque and $M_{y,S}$ vector.

A *Lorenz Messtechnik DR2112-R* torque meter (measurement uncertainty ± 0.002 Nm) is used to measure the torque Q_{TM} supplied by the generator. Due to friction in the bearings and slip ring, the torque measured by the torque meter is smaller than the one measured by the strain gauges on the shaft, but it shows a better signal-to-noise ratio. To obtain an accurate, friction-free, low-noise measurement of mechanical torque, the following method is employed. The friction, which depends on various factors and can vary over time due to temperature and wear, is estimated by calculating the difference $Q_S - Q_{TM}$. This estimate is filtered by a high-order, low-cut-off frequency filter to eliminate noise even at low frequencies. The resulting signal is added to the torque meter measurement to compute Q_{Meas} , which is the torque measurement used by the control system (see Sect. 2.2.6) and logged in the machine data.

2.2.3 Sensors calibration

Before each experimental campaign, all G1 sensors are calibrated in the laboratory or in the wind tunnel, as explained below.

The load cells on the shaft and tower base are calibrated in the lab using weights whose mass is known with an accuracy of ± 0.1 g. During the calibration of the shaft sensors, the drive train is locked in four different azimuth positions; through a bar fixed to the hub, the weights are hung at varying distances from the axis of rotation to simultaneously stress the strain gauges with torsion and bending (Campagnolo, 2013). Similarly, the base of the tower is fixed to a wall, with the EW axis



(or the SS axis when using the fast actuator) aligned in 4 directions relative to the vertical. The azimuth of the rotor and the angular position of the tower are measured with a *Wylcr Clinotronic PLUS* inclinometer (accuracy ≤ 3 arcmin), while the load application arm with respect to the load cell is estimated from the CAD model of the G1 (accuracy ± 0.2 mm). The calibration matrix – 3x3 and 2x2 for the load cells on the shaft and tower base, respectively – is identified by least-squares using the voltage measured downstream of the entire measurement chain.

The measurement of the blade pitch is calibrated in the lab by placing the inclinometer on a CNC-machined saddle that fits onto the blade at a specific and unique span-wise location. With the blade connected to the hub and kept parallel to the ground, the blade pitch is varied using its actuator, and the inclinometer and encoder readings are recorded. The slope of their interpolating line provides a measure of the relationship between the blade pitch and the encoder pulses, yielding a more accurate estimate than one derived from the nominal gearhead ratio and the encoder PPR. The pitch at which the Hall sensor detects zero magnetic flux is also measured using the same setup.

The azimuth angle and the yaw angle in the standard yaw actuator are derived using the nominal PPR values of the corresponding encoders. When using the fast actuator, the yaw angle calculation also accounts for the gearhead nominal reduction ratio. Finally, the rotor speed is obtained using the torque actuator nominal gear ratio and encoder PPR.

As most calibration factors and matrices vary from machine to machine, they are stored on turbine-specific USB sticks. During the wind tunnel experiments, each USB stick is connected to the acquisition and control hardware of the corresponding G1. When the system boots up, the calibration parameters are acquired and stored in internal memory for real-time conversion of voltages and pulses into the corresponding physical quantities.

2.2.4 Acquisition and control hardware

Each G1 is controlled in real time by a Programmable Logic Controller (PLC) *Bachmann MI* (Bachmann electronic GmbH, 2025).

A 16-bit analog acquisition module *AIO216* acquires the strain-gauge signals, appropriately conditioned by dedicated electronic boards located on the rotor and at the tower base, together with the torque-meter signal, the dynamic pressure measured by the Pitot tube transducer, and the turntable position.

An additional *AIO216* module is used to provide the analog set point of the generator current to the *ESCON 50/5* servo controller and to acquire the rotor speed. In particular, the generator current is managed by a control algorithm implemented on the *MI*, as described in Campagnolo (2013). This algorithm uses Q_{Meas} as feedback and regulates the generator current so that the generator supplies the torque requested by the control algorithm responsible for tracking the regulation trajectory (see Sect. 2.2.6).

The azimuth is acquired by a *CNT204/R* module. The blade pitch and nacelle yaw angles are transmitted by the *EPOS2* in digital format via the CANopen protocol. A *CM202* module is used to connect the *EPOS2* to the *MI* controller: it reads the pitch and yaw angles and transmits the set points $\beta_{i, Dem}$ (the desired pitch of the i -th blade) and $\gamma_{nac, Dem}$ (the desired nacelle yaw).



The system operates at different acquisition frequencies. The *MI* controller internal time, the bending moments on the shaft, the torque meter measurement, and the azimuth are acquired every 0.4 ms, i.e. with a sampling frequency f_S equal to 2.5 KHz. Conversely, the rotor speed, tower base loads, measured and demanded pitch and yaw angles, Pitot dynamic pressure, and turntable position are acquired every 4 ms ($f_S = 250$ Hz). The demanded curtailment or derating (see Sect. 2.2.5) is acquired every 8 ms (f_S equal to 125 Hz). The density, obtained from the wind tunnel acquisition system, is considered constant during a single test, which usually lasts a few minutes. It is therefore logged manually by the user as a scalar. The data are written to binary files on the USB stick connected to the *MI*.

A computer in the control room is connected via Ethernet to the *MI*s and used to manage the machines and display the real-time measurements from the main sensors.

240 2.2.5 Regulation trajectories

The regulation trajectories are calculated offline using estimates of the power coefficient (C_P) provided by a simulation model of the G1 implemented in OpenFast (see Sect. 5.4).

The nominal regulation trajectory, shown in Fig. 4 using black lines and circles, maximizes the power produced by the machine for wind speeds below the rated one (region II), whereas it limits the power to the rated value $P_R = 46$ W for higher wind speeds (region III). The calculation of this trajectory takes into account that the power coefficient, which depends on the chord-based Reynolds number, decreases at lower wind speeds (Campagnolo et al., 2020b). Moreover, the optimal tip speed ratio (TSR, noted λ) is set in the range 8.15-8.5, which are typical values for full-scale turbines. In region II, this results in a constant optimal pitch β_{opt} equal to 0.42° , a rotor speed that varies linearly with wind speed, and a torque that is scheduled as a function of the rotor speed, i.e. $Q_{Dem} = f_Q(\Omega)$.

250 The G1 can be down-regulated (or curtailed) in order to limit the power output to a given value $P_D \leq P_R$. Among the various approaches proposed in the literature, the G1 implements the *Const- Ω* strategy (Lio et al., 2018). From the nominal regulation trajectory, the rotation speed corresponding to the desired power level P_D is identified and set equal to Ω_R . The resulting rated torque is P_D/Ω_R . Curtailed trajectories differ from the nominal one only for wind speeds higher than the value required to produce P_D , as shown in Fig. 4a-c.

255 The G1 can also be derated, i.e. it can deliver a power that is a fraction $P_d \leq 100\%$ of what is produced by following the nominal regulation trajectory, regardless of wind speed. Among the various approaches proposed in the literature (Juangarcia et al., 2018; Croce et al., 2024), the G1 strategy maintains the TSR constant. It follows that the rotor speed does not depend on derating, and that the generator torque is reduced according to the derating factor, i.e. $Q_{Dem} = f_Q(\Omega) P_d$. The optimal blade pitch in region II is determined by balancing electrical and aerodynamic power. Due to the dependence of aerodynamic performance on chord-based Reynolds, the desired derating in region II can only be achieved if the fine pitch varies slightly with wind speed. The plots in Fig. 4d-f show the regulation trajectories for different values of P_d , computed using the OpenFast model of the G1.

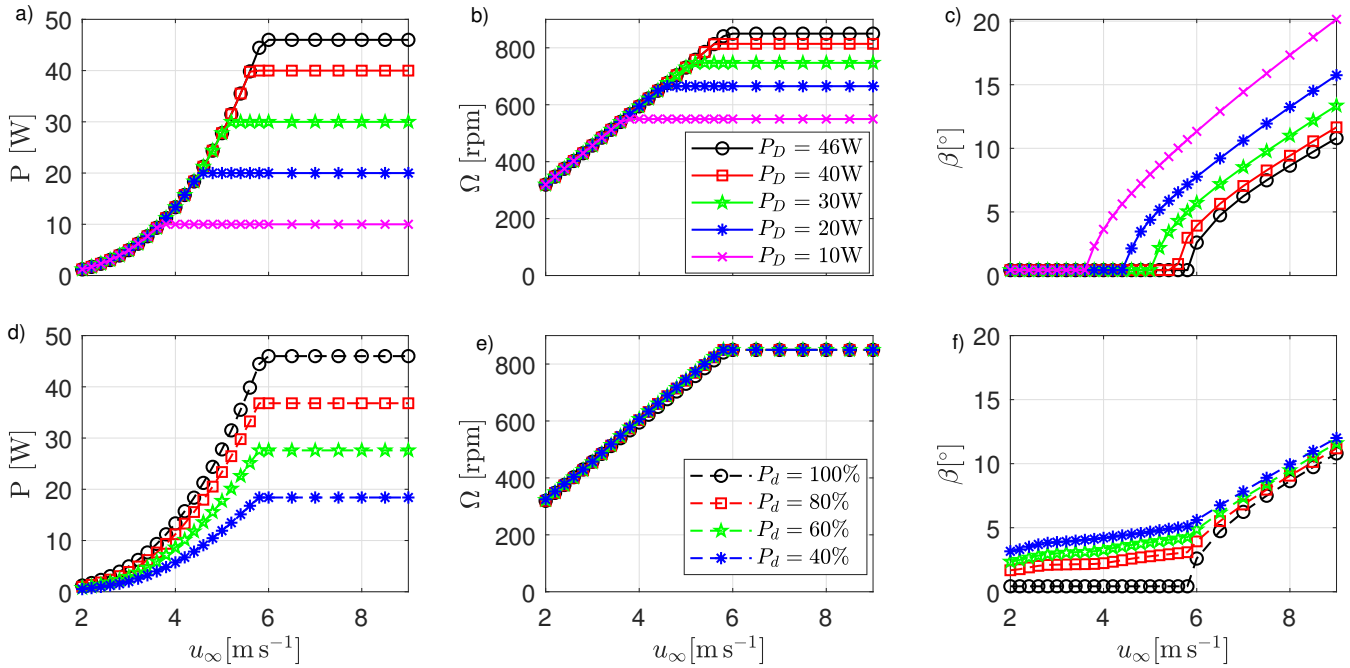


Figure 4. Regulation trajectories tracked by the G1 control algorithm with a density $\rho = 1.19 \text{ Kg m}^{-3}$. The nominal regulation trajectory is depicted by black lines and circles ($P_D = 46 \text{ W}$ and $P_d = 100\%$). Curtailed and derated regulation trajectories are shown in panels **a-c** and **d-f**, respectively.

2.2.6 Control software

The control system, developed in Simulink (The MathWorks Inc., 2023), implements closed-loop algorithms designed to track the regulation trajectories, as well as the wake-mixing strategies Helix, Dynamic Yaw, and Pulse. The control is executed on the *MI* every 4 ms.

The torque and pitch controls that track the desired regulation trajectory were developed in collaboration with the National Kangwon University, and are based on the work of Nam (2013). The torque control consists of a lookup table (LUT) of optimal torque for region II, scheduled based on rotor speed and derating. The torque is saturated at the rated value Q_R , which depends on the curtailment or derating. A correction term, based on a proportional-integral (PI) loop that feeds back on the error $\epsilon_\Omega = \Omega - \Omega_R$, is added to the optimal torque to improve control behavior during the transition between below and above rated conditions. The pitch control consists of a PI loop that feeds back on ϵ_Ω , with Ω_R depending on the curtailment. The pitch is saturated at the fine value β_{opt} , scheduled according to the rotor speed – to account for Reynolds dependency of aerodynamic characteristics – and the derating level. A mode-switch block determines the machine operating status (above or below rated) based on filtered measurements of power, rotation speed, and blade pitch. The gains of the controllers were tuned using a numerical model of the G1 drive train and tower north-south dynamics implemented in Simulink (see Sect. 5.3). The resulting gains are $K_{\beta,P} = 0.0336 \text{ s}$ and $K_{\beta,I} = 0.0168$ for the pitch controller, $K_{Q,P} = 0.00113 \text{ Nms}$ and $K_{Q,I} = 0.000564 \text{ Nm}$ for



the torque controller. In January 2019, the integral gain of the torque controller ($K_{Q,I}$) was set to 0.00282 Nm to improve the performance of the machine under conditions characterized by rapid, significant changes in wind speed.

280 Flags are used to enable the curtailment or derating of the G1, as well as for activating the following wake mixing strategies:

- **Helix**: the i -th blade set-point is equal to

$$\beta_{i,\text{Dem}}(t) = \beta_{\text{opt}} + \hat{\beta}_{\text{Helix}} \sin(f_{\text{Helix}} 2\pi f_r t - 2\pi/3(i-1)), \quad (1)$$

where $\hat{\beta}_{\text{Helix}}$ and f_{Helix} are the Helix amplitude and excitation frequency, expressed in fractions of the rotational frequency f_r . A clockwise (CW) Helix is obtained if $f_{\text{Helix}} < 1$, a counter-clockwise (CCW) Helix if $f_{\text{Helix}} > 1$ (Mühle
285 et al., 2024).

- **Dynamic Yaw**, or **DY**: the nacelle yaw set-point is equal to

$$\gamma_{\text{nac, Dem}}(t) = \hat{\gamma}_{\text{DY}} \sin(2\pi f_{\text{DY}} t), \quad (2)$$

where $\hat{\gamma}_{\text{DY}}$ and f_{DY} are the DY amplitude and excitation frequency, respectively.

- **Pulse**, or **DIC**: the collective blade pitch set-point is equal to

$$\beta_{c,\text{Dem}}(t) = \beta_{\text{DIC}} + \hat{\beta}_{\text{DIC}} \sin(2\pi f_{\text{DIC}} t), \quad (3)$$

where $\hat{\beta}_{\text{DIC}}$ and f_{DIC} are the Pulse amplitude and excitation frequency, respectively, and β_{DIC} is the mean pitch angle.

The controller allows changing the steady yaw set point $\bar{\gamma}_{\text{nac, Dem}}$ while limiting the yaw rate to $\dot{\gamma}_{\text{max}}$. The yaw set point can be implemented even when a wake-mixing strategy is active or when the machine is curtailed/derated, thus combining wake steering with wake mixing or induction control.

295 Finally, load reduction is achieved through an individual-pitch-control (IPC) algorithm (Bossanyi, 2003). The IPC scheme is based on two PI controllers that feed back on the projections of the shaft loads $M_{y,S}$ and $M_{x,S}$ onto a fixed reference frame. The resulting load signals are properly filtered using a low-pass filter prior to control action. Finally, the control request accounts for the delay introduced by the pitch actuator dynamics, as described in Petrović and Campagnolo (2013).

2.3 Hot-wire CTA probes

300 Flow measurements were carried out using tri-axial hot-wire CTA *Dantec 55R91* probes, consisting of three fiber-film sensors, each perpendicular to the others. The sensors form an orthogonal system with an acceptance cone of 70.4° , and are connected to a 6-channel *Dantec StreamLine Pro* anemometric system. The latter is connected to a National Instruments PXI System (National Instruments, 2024), which samples the data at 0.5 ms ($f_S = 2$ kHz) and stores them in internal memory.

The hot-wire probes are calibrated in an open-circuit wind tunnel of the Aerodynamics Laboratory at POLIMI (Politecnico
305 di Milano, 2025), whose test section is 150 mm wide and 200 mm high. The inlet contraction ratio is 25, while the maximum speed is 100 ms^{-1} . The wind tunnel flow velocity is calculated by measuring the dynamic pressure with a pressure transducer



310 *DRUCK LPM9481* (accuracy ± 0.5 Pa), while the density is derived from the measurement of the atmospheric pressure, relative humidity, and temperature. The probe is mounted on its support, whose attitude with respect to the wind tunnel flow is precisely measured by a dual-axis inclinometer *SPECTRON L-212T*. The probes are calibrated with respect to Reynolds number and velocity direction. The calibration procedure accounts for the effects of flow temperature, relative humidity, and absolute pressure, as described by Raffel et al. (2011).



Figure 5. Traversing system equipped with two CTA probes, each one measuring the three components of the velocity vector \mathbf{u} along the longitudinal (u_x), lateral (u_y), and vertical (u_z) directions.

315 Measurements in the boundary-layer test section are performed using two probes supported by a double-pronged sting. The latter, in turn, is attached to a two-axis traversing system, as shown in Fig. 5, and is precisely aligned to the inflow direction using an inclinometer. This setup enables automated movement of the probes along the vertical and lateral axes. The traversing system can be positioned anywhere within the test section, allowing the mapping of the undisturbed inflow or of the wake shed by the scaled wind turbines. The position of each probe within the traversing system is measured using the encoders present in the electrical motors of the two linear actuators. Given the position of the traversing system, it is possible to reconstruct the position of the probes with respect to the reference system shown in Fig. 1a. The three speed components u_x , u_y , and u_z of the velocity vector \mathbf{u} are measured in the reference system shown in Fig. 5.

320 2.4 Lidars

325 Measurements of the undisturbed inflow and of the wakes shed by 3 GIs were also taken using two short-range WindScanner lidars (Mikkelsen et al., 2012), named R2D2 and R2D3. The lidar head scans were positioned as shown in Fig. 1b: R2D2 at $x = -12.516$ m, $y = 6.361$ m, $z = 1.306$ m; R2D3 at $x = -12.526$ m, $y = -6.342$ m, $z = 1.298$ m. Each lidar measures v_{LOS} , i.e. the projection of \mathbf{u} on the lidar line of sight, with a sampling frequency $f_S = 390$ Hz. The two time- and space-synchronized measurements of v_{LOS} provided by the lidars are used to estimate the u_x and u_y components of the wind speed. The experimental setup, its calibration, the data acquisition, and its post-processing are described in detail in van Dooren et al. (2017). For the dataset described in this article, the measurements were resampled at $f_S = 250$ Hz.



3 Execution of the wind tunnel experiments, data post-processing, and measurement uncertainties

This section describes the procedures followed during the execution of the experiments, including the assembly of the experimental setup, the zeroing of the sensors, the synchronization of the data, their post-processing, and, finally, the estimation of measurement uncertainties.

3.1 Assembly of the experimental setup

The experimental setup, including the G1 wind turbines, the Pitot tube placed upstream of the cluster, and, when necessary, the CTA probes with their traversing system or the lidars, is assembled in the test section at the beginning of an experimental campaign, and possibly later modified as necessary depending on the test matrix. The assembly is carried out with the rotating table set to zero degrees. The entire setup is positioned at the desired locations, defined by their coordinates $[x, y, z]$ in the reference system shown in Fig. 1a. To this aim, a longitudinal line parallel to the inflow direction is traced onto the floor of the test section using a multi-line laser level *Huepar LS41G* positioned at the center of the turntable. Using a measuring tape, points are marked at the x coordinates. Centering the laser level at these points, transverse lines are drawn, on which points are marked at the y coordinates. When positioning the wind speed sensing probes, the laser level is centered at the coordinates $[x, y]$, and the head of the Pitot tube or the CTA probe is placed at the desired z coordinate using a measuring stick. The laser level is also used to align the G1 base with the incoming inflow. For information on lidar positioning, please refer to van Dooren et al. (2017).

The G1 turbines are mounted on heavy steel interface plates (thickness: 25 mm, mass > 100 kg) that are, in turn, fixed to the wooden floor of the turntable. Experimental verification confirmed that this mounting configuration does not affect the model natural frequencies. The PLCs that control the G1s, the traversing control system, and the acquisition system of the CTA probes are positioned inside the test chamber, close to the side walls and therefore sufficiently distant (at least 4-5 D) from the experimental setup. Their impact on the flow impinging on the G1s and on the wakes they shed is negligible.

3.2 Zeroing the sensors

Most of the G1 sensors and other sensors (CTA probes, turntable position, etc.) are reset when there is no wind in the test section, and the rotating table is set to 0° . Specifically, the G1 pitch actuator encoder is reset when the PLC is started or rebooted, using the homing procedure described in Sect. 2.2.1. The encoder that measures the nacelle yaw is reset as follows. Once the G1 installation is complete, the yaw actuator is moved until the index channel is detected by its encoder. At this point, the encoder is reset, and the actuator is moved in the opposite direction until the rotor axis is precisely aligned with the inflow direction, using the multi-line laser for the purpose. The yaw angle read by the encoder in this condition is then saved on the G1 USB stick. Each time the PLC is started, an automated homing procedure is performed: (i) the yaw is varied until the index is detected; (ii) the nacelle is then rotated in the opposite direction by an angle equal to the value stored on the USB stick; (iii) the encoder is reset.



Some sensors are subject to measurement drift and must be frequently reset, usually before and after each test run. The
360 torque meter, the Pitot transducer, the analog signal that carries the turntable position, and the CTA probes are reset with the
G1 actuators disabled. The sensors at the tower base are reset by keeping the nacelle yaw at zero ($\gamma_{nac} = 0^\circ$) and the rotor
standing still. The tower loads are therefore corrected for the gravitational loads induced by the masses of the tower and rotor-
nacelle assembly in the configuration $\gamma_{nac} = 0^\circ$. The load induced by the rotor-nacelle assembly is particularly significant,
given that its center of gravity is quite offset from the tower axis. The load sensors on the shaft are reset as follows: several
365 rotor rotations are performed at very low speed ($\Omega < 30$ rpm), with the load cell measuring solely zero-mean gravitational
loads. The average values read by the sensors are stored in internal memory and subtracted from subsequent measurements in
real time.

The encoder that reads the azimuth is reset via software every time its index channel is detected. Once the G1 has been
assembled in the wind tunnel, the rotor is manually rotated a few times to ensure that the index channel is detected. The rotor
370 is then set to zero azimuth using a laser level. The value of ψ in this position is stored on the USB stick and subtracted in real
time from subsequent measurements.

The zeroing of hot-wire probes is performed with the wind tunnel off. For the reset of the lidars, please refer to van Dooren
et al. (2017).

3.3 Test execution and data synchronization

375 The tests are conducted according to a specific test matrix. Once the desired environmental conditions (wind speed and turntable
angle) and the operating conditions of the G1s (control type and related settings) have been set, a few seconds are allowed for
the wakes to develop and for the response of the machines to stabilize. Data acquisition then proceeds for the required duration.

The data acquired from the G1s is synchronized as follows. A MATLAB script, executed on the computer that manages
the G1s, simultaneously sends a request to start acquisition on all *MI*s via the Modbus protocol; the maximum expected
380 desynchronization is less than 10 ms. Synchronization between G1 and CTA probe data is achieved by orally synchronizing
the start of the respective acquisitions; the expected desynchronization is in the order of 1 s. Synchronization between G1
and lidar data is achieved through postprocessing: during the experiments, the acquisition systems of the upstream G1 and the
lidars both acquire the same trigger signal, generated by a third source; the maximum expected desynchronization is less than
the sample time, i.e. 4 ms.

385 3.4 Data post-processing

The binary data of the G1s and of the flow probes are converted into the format presented in Sect. 4.2 and saved to *NetCDF* files
using Matlab scripts. Most measurements are saved as they are recorded. The measurements of rotor speed and shaft torque
are instead first filtered using a forward-backward eighth-order low-pass Butterworth filter (pass-band equal to three times the
average rotational frequency), and then saved in the *NetCDF* files. Power is calculated as the product of these two physical
390 quantities, with the torque downsampled to 250 Hz.



3.4.1 Post-processing of flow measurements

Post-processing of the hot-wire probe data consists of transforming, via the calibration matrix, the voltages measured by the acquisition system into the three velocity components. The resulting data are then corrected as follows. At the beginning of a measurement campaign, the flow is sampled along a horizontal line at hub height with the turbines not installed in the wind tunnel, i.e. under conditions such that the mean flow can be considered aligned with the longitudinal direction. For each acquisition point, the yaw angle $\gamma_{\mathbf{u}} = \text{atan2}(u_y, u_x)$ and the tilt angle $\varphi_{\mathbf{u}} = \text{atan2}(u_z, \sqrt{u_x^2 + u_y^2})$ of the mean velocity vector are computed. Any deviation from zero is attributed to imperfect levelling of the measurement system – including the traversing unit, the probes, and their support – rather than to small elastic deformations during motion. During post-processing, the average yaw and tilt estimated in this preliminary scan are subtracted from the corresponding angles measured during the campaign. The time history of the velocity vector is then reconstructed. This correction assumes that the yaw and tilt biases are stationary throughout the measurement campaign and independent of the flow conditions, which is reasonable given the relatively low wind speeds of the test.

For the post-processing of the lidar data, please refer to van Dooren et al. (2017).

3.4.2 Post-processing to compensate for strain-gauge torque drifts

In a few experiments at sub-rated wind speeds, discrepancies of up to 15% of Q_R were observed between measurements of Q_S at two consecutive zeroings due to malfunctioning of the strain gauges conditioning boards. This indicates a drift in the measurement chain during data acquisition, compromising the accuracy of the mechanical torque signal. Because this signal is used as feedback by the generator current controller (see Sect. 2.2.2), the actual generator torque deviates from the target value Q_{Dem} by an amount comparable to the drift. Consequently, G1 settles at a rotational speed – and thus a TSR – different from the intended operating point. This leads to operation at a C_P different from the expected value and to an inaccurate computation of the reference torque. A simple algebraic correction of the measured torque by adding or subtracting the estimated drift is therefore not sufficient. The thrust coefficient C_T , on the other hand, is only marginally affected, owing to its low sensitivity to TSR in region II.

In such cases, torque and speed measurements were corrected during post-processing as follows. A Simulink model of the drive-train and tower NS dynamics (see Sect. 5.3) was used to perform simulations with turbulent wind fields with mean speeds between the cut-in and rated values. The generator torque was artificially biased within $\pm 15\%Q_R$ to reproduce the effect of the drift on the closed-loop dynamics. For each simulation, differences in the mean mechanical torque and rotational speed with respect to the unbiased case, denoted ΔQ and $\Delta\Omega$, were stored in a LUT parameterized by the imposed bias and the mean rotational speed. The drift during each experiment was estimated assuming it varies linearly with time and then used, together with the measured rotational speed, to interpolate the LUT. The interpolated values were finally used to correct the measured torque and speed. The resulting time series are filtered as explained above, and then saved in the *NetCDF* files.

A comparison between experiments conducted under the same environmental and operating conditions, some with torque signal drift and others without, highlighted the validity of the developed correction method, even in the presence of significant



drift. In particular, the measured power is consistent with variations within the expected measurement uncertainty. For exper-
425 iments affected by torque signal drift, however, there is a discrepancy between the rotation speed recorded in the data and the
rotation speed that can be calculated by differentiating the azimuth or inferred from the shaft load spectrum.

3.4.3 Post-processing to compensate for rotor imbalances

The G1 rotor exhibits small but non-negligible inertial and aerodynamic imbalances. The inertial imbalance originates from
minor mass asymmetries among the blades and from the non-uniform azimuthal and radial distribution of wiring in the hub
430 region (see Fig. 3, top). The aerodynamic imbalance reflects both deviations of the blade geometry from the nominal profile
due to manufacturing tolerances (Campagnolo, 2013) and the uncertainty in blade pitch measurement (see Sect. 3.6) used
as feedback by the pitch actuator, resulting in slightly different pitch settings among the blades. These imbalances affect
the bending moments measured on the rotor and tower: the mean rotor-side moments deviate from zero, whereas the tower-
base moments exhibit a pronounced component at the rotational frequency (f_r , or 1P). The measurements are corrected as
435 follows. The shaft-side moments are first projected onto a fixed reference frame using the rotor azimuth; the 1P component is
then removed by demodulating the time series over a moving window spanning one rotor revolution; the corrected moments
are finally projected back onto the rotating frame. Tower-base moments are similarly corrected for the 1P component by
demodulating the raw signals. Both the original and corrected loads are stored in the *NetCDF* files.

3.5 Derivable physical quantities

440 The signals measured during the experiments can be used to derive other physical quantities.

At a fixed wind-tunnel fan rotational speed, the mean wind speed measured by the Pitot probe may vary slightly between
tests due to the turbulent nature of the flow. For this reason, the turbine performance is usually analysed in terms of normalised
power, defined as $P_n = 2\bar{P}/(\rho A \bar{u}_\infty^3)$, where \bar{P} is the mean mechanical power measured at the shaft, A is the rotor disk area,
and \bar{u}_∞ the mean Pitot wind speed. The normalised power of the upstream turbine (WT1) corresponds to its power coefficient,
445 C_P . For the downstream turbines operating in the wake, the normalised power differs from C_P , as discussed in Campagnolo
et al. (2020b).

The moments measured on the rotating shaft can be projected onto the fixed reference frame, thus obtaining the nodding
(tilt) moment Nod_F and the yawing moment Y_{aw_F} acting on the nacelle. These moments are stored in the *NetCDF* files after
being corrected for the effects of the inertial and aerodynamic imbalance of the rotor, and for the contribution of the rotor
450 weight.

The moments measured at the tower base can be used to estimate the thrust coefficient, defined as $C_T = 2\bar{T}/(\rho A \bar{u}_\infty^2)$, with
 \bar{T} the mean thrust along the rotor axis. Estimating \bar{T} is also possible if the rotor is yawed, and requires correcting the loads for
(i) the yaw-dependent drag of the nacelle and tower, and (ii) the variations of gravitational loads for $\gamma_{\text{nac}} \neq 0^\circ$.



$\mathbf{R}(\cdot)$ denoting the 2D rotation matrix.

The projection of the corrected loads onto a reference frame aligned with the rotor axis yields

$$475 \quad \mathbf{m}_{\text{RA,cor}} = \mathbf{R}(-\gamma)\mathbf{m}_{\text{cor}}, \quad (7)$$

with $\mathbf{m}_{\text{RA,cor}} = [\text{FA}_{\text{cor}}; \text{SS}_{\text{cor}}]$. The thrust is finally obtained as $T = -\text{FA}_{\text{cor}}/z_{\text{SG}}$, with z_{SG} the elevation of the rotor axis above the strain-gauge section (see Fig. 3, bottom).

If the fast yaw actuator is used, the reconstruction simplifies considerably. In this case, the sensors at tower base rotate with the nacelle and are already corrected for gravitational loads during their zeroing (see Sect. 3.2); no additional gravitational
480 correction is therefore required. The corrected fore-aft and side-side moments are obtained as

$$\mathbf{m}_{\text{RA,cor}} = \mathbf{m}_{\text{RA}} - \mathbf{R}(-\gamma)\mathbf{d}_{\text{NT}}, \quad (8)$$

with $\mathbf{m}_{\text{RA}} = [\text{FA}; \text{SS}]$ the raw tower-base bending moment vector.

Previous publications (Campagnolo et al., 2020b; Campagnolo and Bottasso, 2021; Campagnolo et al., 2022a; Mühle et al., 2024) have investigated Damage Equivalent Loads (DELs) collected on the G1 turbine. Therein, the DELs are calculated using
485 the rainflow counting algorithm implemented in Matlab (The MathWorks Inc., 2023) and the Palmgren-Miners rule (Miner, 1945). The equivalent number of cycles is defined as the product of the load signal duration and the rated rotor speed of the nominal regulation trajectory ($\Omega_{\text{R}} = 850$ rpm). In this way, it is possible to directly compare DELs calculated from time histories of different durations. The slope of the S-N curve is set to $m = 10$ for tower-based loads and hub loads projected onto the fixed frame, and $m = 4$ for rotating loads, as the latter are assumed to be representative of the fatigue loads experienced
490 by composite blades. For computing the DELs, load signals are filtered above six times the rotor frequency (6P), to remove high-frequency load components. Combined DELs may also be obtained by projecting the two orthogonal load components on the direction associated with the maximum DEL. Finally, normalized DELs are computed as $\text{DEL}_{\text{n}} = 2\text{DEL}/(\rho A R \bar{u}_{\infty}^2)$.

The torque, Nod_{F} and Yaw_{F} moments can be used to estimate the Rotor Effective Wind Speed (REWS) and the effective wind speed on four equally sized, 90° -wide sectors, as described in Schreiber et al. (2020b). For this purpose, it is necessary
495 to use a mapping of the power and cone (C_{m} , defined in Bottasso et al., 2018) coefficients, which can be derived using the OpenFast model of the G1 (see Sect. 5.4). A validation of this method against lidar data is discussed in Campagnolo et al. (2017).

3.6 Assessment of the measurement uncertainties

The sensors of the experimental setup measure physical quantities affected by uncertainty, classifiable according to their
500 respective sources, namely:

- **Linearity**: associated with the linearity of the calibration model. In this work, the standard deviation of the residuals with respect to the calibration line is used to estimate the uncertainty, consistent with the guidelines of ISO and OIML (1993).



- **Resolution:** due to the discrete nature of the measurement output. Assuming a uniform quantization error over the interval $[-\delta/2, +\delta/2]$, the resulting uncertainty for a 95% confidence level is $\Delta = 1.645 \delta / (2\sqrt{3})$, as prescribed in ISO and OIML (1993).
- **Thermal drift:** mainly associated with temperature-induced variations of the sensor output at zero-load (Temperature Effect on Zero, or TEZ).
- **Zeroing:** type B standard uncertainty associated with the definition of the zero position.
- **Backlash:** the yaw encoder of the fast actuation system measures angular position upstream of a gearbox that exhibits mechanical backlash equal to γ_{BL} . Consequently, the encoder reading does not uniquely define the yaw angle in the presence of directional reversals, giving rise to a deadband-type uncertainty for a 95% confidence level equal to $\Delta = 1.645 \gamma_{BL} / \sqrt{3}$.
- **Other:** contributions not included in the categories above.

G1 load transducers are predominantly affected by linearity uncertainty. Figure 7 compares the applied loads (x axis) with those reconstructed through the calibration matrix (y axis) of a G1 unit. The root-mean-square error (RMSE) shown in the plots is used as an estimate of the linearity uncertainty at the intended confidence level. Similar results have been observed across multiple G1 units.

An analysis performed over multiple successive zeroings of the load cells indicated a small thermally-induced drift in the transducer zero, which may lead to inaccurate measurements, as explained in Sect. 3.4. Figure 8 reports the distribution of the variation of the zero offsets between two consecutive zeroing procedures of a G1 unit. The standard deviation obtained from the Gaussian fits is used to quantify the uncertainty at the chosen confidence level. Also in this case, similar results have been observed across multiple G1 units.

Encoder-based measurements are primarily affected by resolution uncertainty. Let N_p denote the PPR of the encoder and i the reduction ratio of any gearbox interposed between the encoder and the body whose rotation angle is to be determined; the corresponding angular resolution is then given by $\delta = 360^\circ / 4N_p i$, as the *CNT204/R* and *EPOS2 24/2* modules implement X4 encoding.

For the encoder measuring the pitch angle, the linearity uncertainty is evaluated from the residuals with respect to the best-fit calibration line obtained from encoder-inclinometer measurements (see Sect. 2.2.3). The resulting RMSE is typically on the order of 0.05° .

The G1 encoders require a zeroing procedure (see Sect. 3.2). The yaw-control and azimuth encoders are zeroed in the wind tunnel using a laser level, with an estimated accuracy on the order of $0.2^\circ - 0.5^\circ$. The pitch encoders are instead zeroed using a Hall sensor calibrated in the laboratory (see Sect. 2.2.3). Several repetitions of the calibration procedure indicate a repeatability of 0.1° .

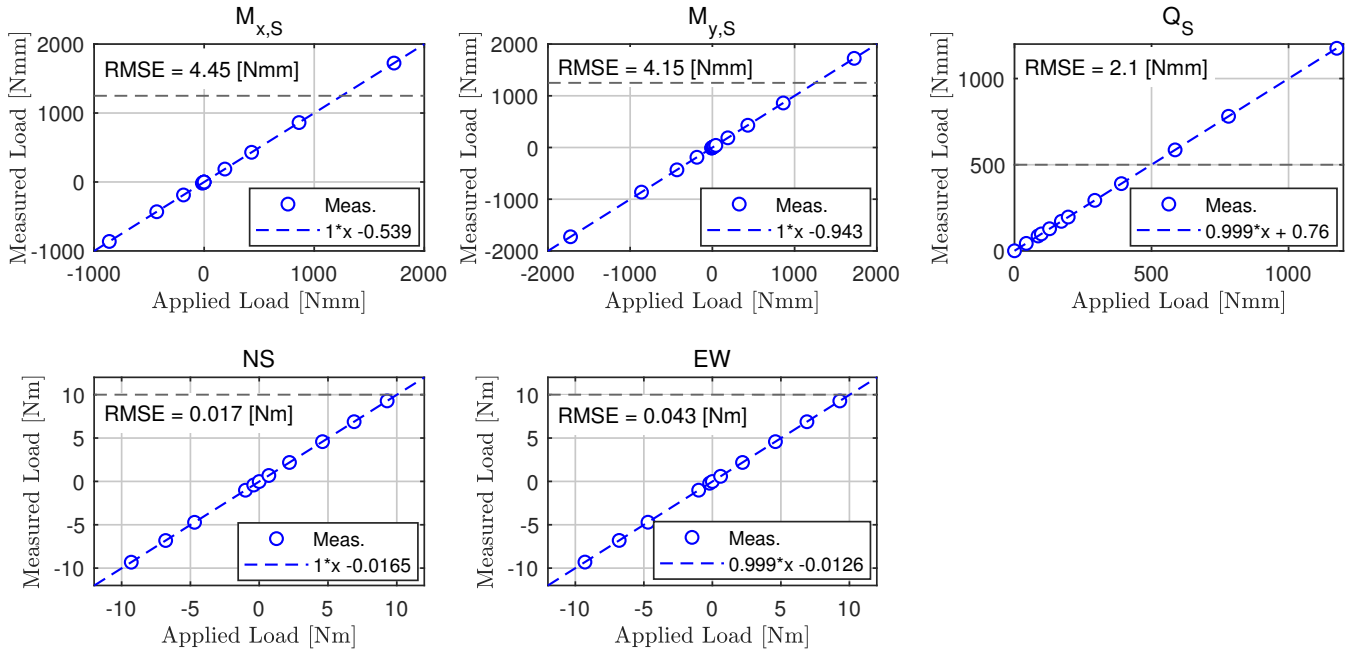


Figure 7. Comparison between applied loads (x axis) and loads reconstructed using the calibration matrix (y axis). The horizontal dotted lines mark the absolute value of the expected loads at the rated wind speed. The plots include the best-fitting line and the RMSE of the residuals.

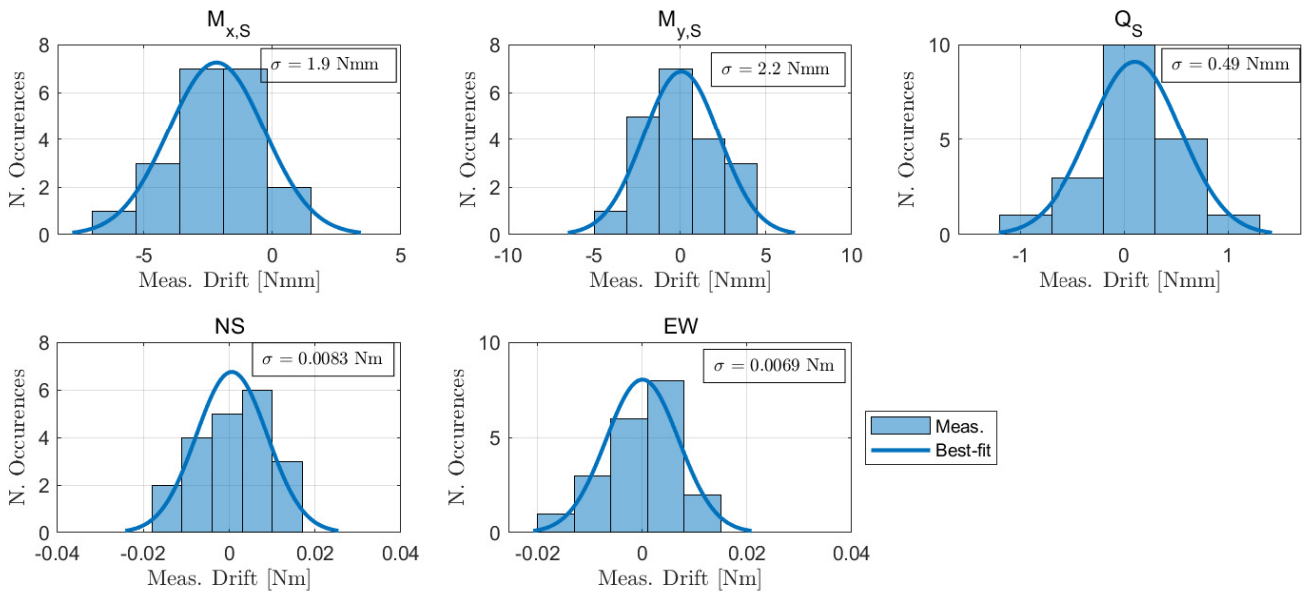


Figure 8. Distribution of the zero drift of the five G1 load sensors between successive zeroing. The plots also include the best-fitting Gaussian, with its standard deviation reported within the text box.



535 The positioning of the devices installed in the wind tunnel is performed using a meter (1-mm resolution) and a laser level (see Sect. 3.1). Repeated positioning tests reveal small variations in the device actual location, which is therefore considered known with an uncertainty of 5 mm.

The uncertainty associated with measuring the rotor angular velocity warrants special consideration. For some G1s, the angular velocity obtained by differentiating the azimuth encoder signal slightly differs from that measured by the torque-
540 actuator encoder. This discrepancy is attributable to a small deviation (up to 0.2%) of the gearbox reduction ratio from its nominal value, due to manufacturing tolerances, and constitutes the dominant source of uncertainty.

Derived physical quantities inherit uncertainties by propagation of the uncertainties of the underlying measured variables. For the density, this results in an expected uncertainty of $\Delta\rho = 0.01 \text{ kg m}^{-3}$.

The uncertainty associated with hot-wire probe measurements under laminar conditions is discussed in Raffel et al. (2011).
545 In turbulent flows, the same authors estimate an uncertainty of 0.1 ms^{-1} on the velocity magnitude $|\mathbf{u}|$, and 0.2° on the tilt and yaw angles. Finally, the uncertainty associated with the lidar measurements is described in detail in van Dooren et al. (2017).

Table 1 provides a summary of the measurement uncertainties at a 95% confidence level. For selected physical quantities, the table reports the uncertainty contributions arising from the sources discussed above. The overall uncertainty (last column) is conservatively estimated as the sum of the individual contributions when these are of comparable magnitude, or as the
550 maximum contribution when one source is dominant.

4 Experimental dataset

This section describes the content of the experimental dataset, the data format, and the provided metadata.

4.1 Dataset content

The content of the experimental dataset is summarized in Table 2. It includes experimental inflow mappings obtained in an
555 empty test section, wake measurements downstream of one, two, or three turbines, and turbine operational data measured for a three-turbine cluster under both stationary and dynamically varying mean wind-direction conditions.

4.1.1 Inflow mapping with empty wind tunnel

Measurements of the inflow were performed with the four ABLs presented in Sect. 2.1.1. The Low-TI was sampled using the lidars along a vertical plane at the turntable center point. The Mod-TI, High-TI, and Extreme-TI ABLs were sampled with the
560 CTA probes 9.94 m upstream of the turntable center point. The inflow mapping was performed along a vertical plane for the Mod-TI and High-TI ABLs, and along a vertical and a horizontal line at hub height for the Extreme-TI.

The dataset (Campagnolo et al., 2026f) consists of time histories of the three velocity components measured by the CTA probes, along with lidar measurements of the mean longitudinal velocity. Figure 9a–c shows the mean longitudinal velocity \bar{u}_x for the Low-TI, Mod-TI, and High-TI ABLs, normalized by the mean longitudinal velocity $\bar{u}_{x,P}$ measured at the reference



Table 1. Uncertainty summary table at a 95% confidence level. For selected physical quantities, the table reports the uncertainty contributions from linearity, resolution, thermal drift, zeroing, backlash, and other sources.

	Physical quantity	Linearity, resolution	Thermal drift, zeroing	Backlash, other	Overall uncertainty
Wind tunnel, and its sensors	Equipment position	0.00047 m	-	0.005 m	$\Delta x = \Delta y = \Delta z = 0.005 \text{ m}$
	Density	-	-	-	$\Delta \rho = 0.01 \text{ kg m}^{-3}$
	Pitot wind speed	-	-	-	$\Delta u_\infty = \frac{1}{\rho u_\infty} \sqrt{(\Delta p_{\text{dyn}})^2 + \frac{u_\infty^4}{4} (\Delta \rho)^2}$
	Turntable angle	0.0052°	-	-	$\Delta \Phi = 0.0052^\circ$
G1 sensors	Blade pitch angle	0.1°	0.1°	-	$\Delta \beta = 0.2^\circ$
	Rotor azimuth	0.017°	0.5°	-	$\Delta \psi = 0.5^\circ$
	Rotor speed	-	-	0.2%Ω	$\Delta \Omega = 0.002 \Omega$
	Nacelle yaw, standard actuator	0.0043°	0.2°	-	$\Delta \gamma_{\text{nac}} = 0.2^\circ$
	Nacelle yaw, fast actuator	0.00085°	0.2°	0.063°	$\Delta \gamma_{\text{nac}} = 0.2^\circ$
	Mechanical torque	0.005 Nmm	0.001 Nm	-	$\Delta Q_{\text{Meas}} = 0.005 \text{ Nm}$
	Mechanical power	-	-	-	$\Delta P = \sqrt{(\Omega \Delta Q_{\text{Meas}})^2 + (Q_{\text{Meas}} \Delta \Omega)^2}$
	Shaft bending moments	0.01 Nm	0.004 Nm	-	$\Delta M_{x,S}, \Delta M_{y,S} = 0.01 \text{ Nm}$
Tower bending moments	0.1 Nm	0.016 Nm	-	$\Delta NS, \Delta EW, \Delta FA, \Delta SS = 0.1 \text{ Nm}$	
CTA probes	Wind vector magnitude	-	-	-	$\Delta \mathbf{u} = 0.1 \text{ ms}^{-1}$
	Wind vector angles	-	-	-	$\Delta \gamma_{\mathbf{u}} = \Delta \varphi_{\mathbf{u}} = 0.2^\circ$
Lidars	Wind speed components	-	-	-	see van Dooren et al. (2017)

Table 2. Overview of the data content included in the experimental dataset, corresponding description, repository, and dataset size.

Dataset content	Dataset content description	Dataset repository	Dataset size
Inflow mapping	see Sect. 4.1.1	https://doi.org/10.5281/zenodo.18749773	2.86 Gb
Single wake measurement	see Sect. 4.1.2	https://doi.org/10.5281/zenodo.18732794	31.88 Gb
Double wakes measurement	see Sect. 4.1.2	https://doi.org/10.5281/zenodo.18743973	41.05 Gb
Multiple wakes measurement	see Sect. 4.1.3	https://doi.org/10.5281/zenodo.18731994	0.67 Gb
Wind turbine data, steady wind direction	see Sect. 4.1.4	https://doi.org/10.5281/zenodo.18723855	110.11 Gb
Wind turbine data, time-varying wind direction	see Sect. 4.1.5	https://doi.org/10.5281/zenodo.18743431	73.38 Gb



565 Pitot position. Figure 9d shows the vertical profiles, measured at the pitot position, of the normalized longitudinal velocity (left) and longitudinal turbulence (right).

The non-homogeneity of the mean flow is evident not only in the vertical direction, but also across the transverse direction, as previously discussed in Schreiber et al. (2020c); Campagnolo et al. (2020b, 2022b). Experimental measurements indicate that this non-homogeneity is only marginally affected by the operating power of the wind tunnel fans, at least within the velocity range relevant to the G1 experiments. Therefore, the inflow mapping can be scaled by multiplying the ratio $\bar{u}_x/\bar{u}_{x,P}$ by the mean velocity measured at the Pitot location during the G1 experiments.

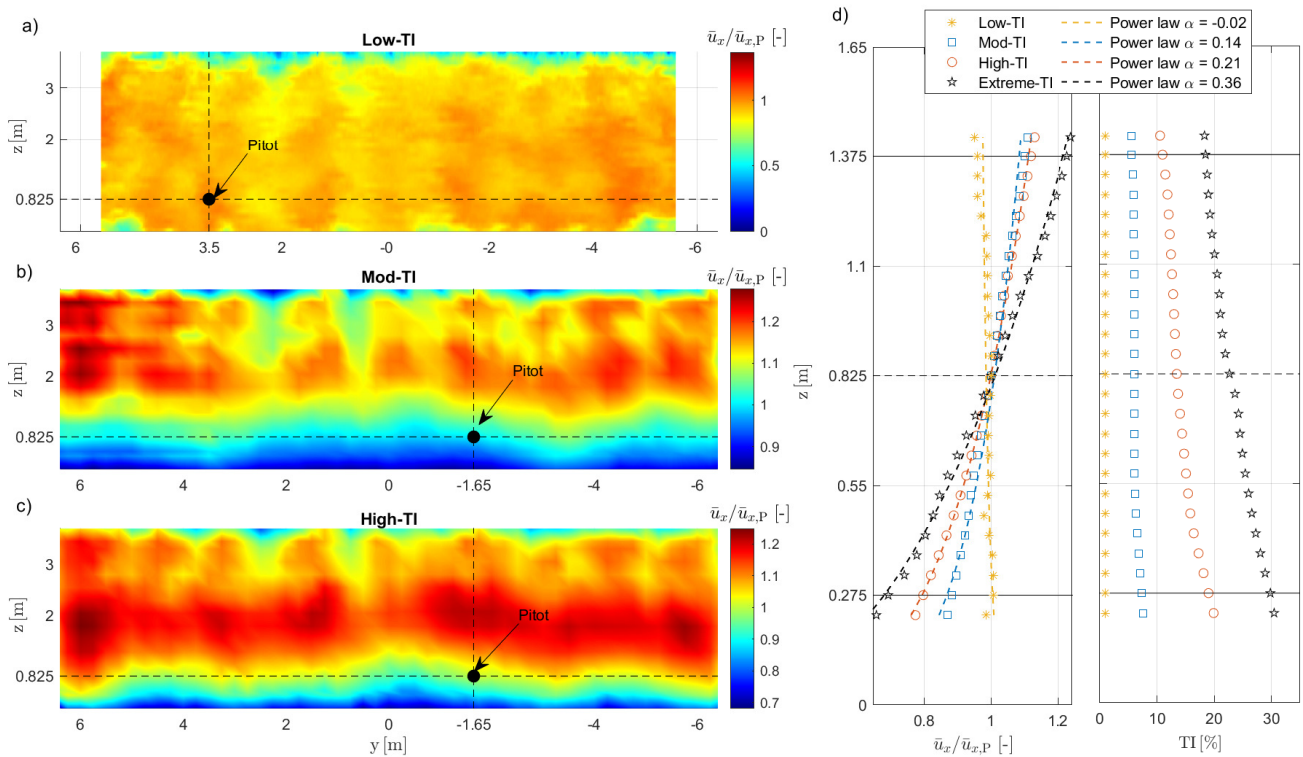


Figure 9. Characteristics of the inflows that were passively generated in the wind tunnel and measured by the lidars or CTA probes: normalized longitudinal wind velocity with Low-TI (a), Mod-TI (b), and High-TI (c) inflows, looking downstream; vertical profiles of the normalized longitudinal wind speed and their best-fitting power laws (d, left), and vertical profiles of the longitudinal turbulence intensity (d, right); within (d), the black dashed line indicates the hub height, while the two solid black lines limit the rotor disk.

The inflow mapping was used to normalize G1 power production in Campagnolo et al. (2020b), whereas it was applied to wake normalization in Wang et al. (2017a).



4.1.2 Measurement of single and double wakes with CTA probes

575 The wake generated by a single G1 or by a tandem of two G1 turbines was measured using CTA probes. Wake measurements were performed along vertical and horizontal lines at various downstream distances from the rotor(s). The G1 turbines were operated under different conditions, including greedy operation, power curtailment, yaw misalignment, Pulse operation, and IPC. Tests were conducted by reproducing the four ABLs described in Sect. 2.1.1.

580 The datasets (Campagnolo et al., 2026c, e) consist of time histories of the three velocity components measured by the CTA probes, along with time series of the corresponding operational data for the G1 turbine(s). These data have been used for the development (Kim et al., 2018; Schreiber et al., 2020a; Zengler et al., 2024) and validation (Schreiber et al., 2017; Ruisi and Bossanyi, 2019; Campagnolo et al., 2019; Schreiber et al., 2020c) of wake engineering models, for the tuning and validation of large-eddy simulation (LES) codes (Wang et al., 2017a, b, 2019), and for assessing the impact of IPC and wake mixing techniques on wake recovery (Wang et al., 2020a, c).

585 4.1.3 Measurement of multiple wakes with lidars

The wake generated by a cluster of three G1 turbines, arranged in a column with longitudinal and lateral spacings of 4D and 0.5D, respectively, was measured using lidars along a horizontal plane located approximately 0.1 m above the hub height. The G1 turbines were operated in both greedy and misaligned modes, and the tests were conducted under Mod-TI inflow conditions.

590 The dataset (Campagnolo et al., 2026b) consists of time series of the line-of-sight, longitudinal, and lateral velocity components measured by the lidars, together with the corresponding operational data of the G1 turbines. These data have been used to assess the reliability of lidar measurements in boundary-layer wind tunnels (van Dooren et al., 2016, 2017) and to validate LES codes (Draper et al., 2018a, b; Wang et al., 2018a, 2020d).

4.1.4 Wind turbine data under steady wind direction

595 Measurements of G1 operational data were performed using a cluster of three turbines arranged in a column, with inter-turbine spacings between 3.2D and 5D. The turbines were operated under a range of conditions, including greedy operation, power curtailment and derating, wake steering, individual pitch control for load reduction, Pulse operation, Helix control, dynamic yaw, as well as combinations of derating, curtailment, Helix, and dynamic yaw with wake steering.

600 Data were collected under the three atmospheric boundary-layer conditions Low-TI, Mod-TI, and High-TI. During each experimental run, the mean wind speed and direction were held constant, and multiple tests were performed to assess the cluster sensitivity to variations in these parameters.

605 The dataset (Campagnolo et al., 2026a) has been used to investigate the effectiveness of several wake control techniques (Campagnolo et al., 2016; Wang et al., 2020c; Frederik et al., 2020b; Campagnolo et al., 2023; Bortolin et al., 2026; Mühle et al., 2026), to develop and validate engineering models of wind farms (Schreiber et al., 2017; Draper et al., 2018b; Schreiber et al., 2020c; Campagnolo et al., 2020b, 2022b), and to develop models that capture the effect on power of the way a turbine is controlled as it is misaligned (Tamaro et al., 2024).



4.1.5 Wind turbine data under dynamically varying wind direction

Measurements were performed using a cluster of three G1 turbines arranged in a column with a spacing of 5D, with the turntable dynamically rotated to reproduce time-varying wind-direction conditions. Figure 10 shows the 90-minute time history of the rotation imposed on the turntable, synthesized to reproduce wind-direction variations observed in real atmospheric
610 conditions (Campagnolo et al., 2020b).

The G1 operational data were collected by testing two classes of control strategies. The first class consists of LUT-based wind-farm control algorithms aimed at boosting cluster power through wake steering. The second class comprises Active Power Control (APC) algorithms (Tamaro et al., 2026) that track a prescribed time-varying reference power level by a combination of curtailment and yaw misalignment. In the former case, the tests were conducted by dividing the wind-direction time history
615 into nine blocks of 10 minutes, as shown in Fig. 10, and by using LUTs computed as described in Campagnolo et al. (2020b). In the latter case, the tests lasted 180 s and were conducted using a portion of the 90-minute time history, highlighted in red and labeled Φ_{APC} in Fig. 10. In both cases, filtered measurements of wind direction were fed to the controllers to determine, in real time, the optimal control settings.

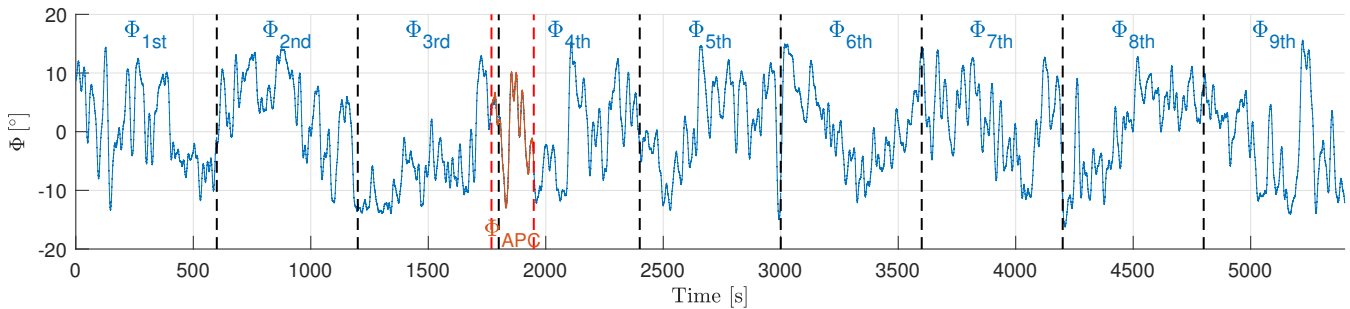


Figure 10. The 90-minute time history of the rotation imposed on the turntable during experiments with dynamically varying wind direction. The 10-minute blocks used for the power-boosting experiments are shown in blue and are separated by vertical black dashed lines. The 180 s block used for the APC experiments, labeled Φ_{APC} , is shown in red.

The dataset (Campagnolo et al., 2026d) consists of time series of operational data from the G1s, as well as the LUTs of the
620 power-boosting wind farm controller. The APC controllers are provided in Tamaro et al. (2025). The data have been used in several research works (Campagnolo et al., 2020a, b; Campagnolo and Bottasso, 2021; Tamaro et al., 2026) to study the effects of control settings on the power production and fatigue loads of the turbine cluster.

4.2 Data format

The data are saved in NetCDF files using the structure described in Table 3. In addition to the measurements from the sensors
625 described in the previous sections, the time elapsed since the start of data acquisition, sampled at 2.5 kHz, is also saved.



Table 3. Structure of the *NetCDF* files storing the G1s, hot-wire CTA probe, and lidars data.

Field	Field description [unit of measurements]	f_s [Hz]
Time	Time vector [s]	2500
WindTunnelData/	Structure array containing wind tunnel recorded data	
PitotVelocity	Pitot wind speed, u_∞ [ms^{-1}]	250
TurntableAngle	Turntable angle, Φ [$^\circ$]	250
AirDensity	Air density, ρ [kg m^{-3}]	scalar
WTsData/	Structure array containing WTs recorded data	
WT1/	Structure array containing WT1 recorded data	
Pitch/		
Blade1	Blade 1 pitch, β_1 [$^\circ$]	250
Blade1Dem	Control-demanded pitch of Blade 1, $\beta_{1,\text{Dem}}$ [$^\circ$]	250
Blade2	Blade 2 pitch, β_2 [$^\circ$]	250
Blade2Dem	Control-demanded pitch of Blade 2, $\beta_{2,\text{Dem}}$ [$^\circ$]	250
Blade3	Blade 3 pitch, β_3 [$^\circ$]	250
Blade3Dem	Control-demanded pitch of Blade 3, $\beta_{3,\text{Dem}}$ [$^\circ$]	250
RotorSpeed	Rotor speed, Ω [rpm]	250
Azimuth	Rotor azimuth, ψ [$^\circ$]	2500
Hub/	Shaft rotating loads	
Torque	Torque, Q_{Meas} [Nm]	2500
Nodding	Moment, $M_{x,S}$ [Nm]	2500
Yawing	Moment, $M_{y,S}$ [Nm]	2500
Tower/	Tower base loads	
NS or FA	North-South (NS) or Fore-Aft (FA) moment [Nm]	250
EW or SS	East-West (EW) or Side-Side (SS) moment [Nm]	250
Power/		
Meas	Mechanical power, P [W]	250
RefAbs	Control-demanded power curtailment, P_D [W]	125
RefRel	Control-demanded power derating, P_d [%]	125
Yaw	Nacelle orientation, γ_{nac} [$^\circ$]	250
YawDem	Control-demanded nacelle orientation, $\gamma_{\text{nac,Dem}}$ [$^\circ$]	250
FilteredLoads/	Loads corrected for the effect of rotor imbalance (see Sect. 3.4)	
Hub/		

Continued on next page



Field	Field description [unit of measurements]	f_s [Hz]
Nodding	Shaft rotating moment, $M_{x,S}$ [Nm]	2500
Yawing	Shaft rotating moment, $M_{y,S}$ [Nm]	2500
NoddingFixed	Fixed frame Nodding (Tilt) moment, Nod_F [Nm]	2500
YawingFixed	Fixed frame Yawing moment, Yaw_F [Nm]	2500
Tower/		
NS or FA	North-South (NS) or Fore-Aft (FA) moment [Nm]	250
EW or SS	East-West (EW) or Side-Side (SS) moment [Nm]	250
WT2/	Structure array containing WT2 recorded data (if WT2 was ON during the test)	
WT3/	Structure array containing WT3 recorded data (if WT3 was ON during the test)	
FlowData/	Structure array containing flow data sampled at N different positions with the CTA probes. It only exists if flow measurements with CTA probes were conducted during the test	
Probe1/	Structure array of flow data sampled at the 1 st probe position	
InitTime	Flow sampling at different points is done sequentially. This field reports the elapsed time since the beginning of the WT(s) data acquisition [s]	scalar
Position/	Probe position	
x	coordinate x [mm]	scalar
y	coordinate y [mm]	scalar
z	coordinate z [mm]	scalar
ux	u_x component of the wind speed [ms^{-1}]	2000
uy	u_y component of the wind speed [ms^{-1}]	2000
uz	u_z component of the wind speed [ms^{-1}]	2000
Probe2/	Structure array of flow data sampled at the 2 nd probe position	
⋮		
ProbeN/	Structure array of flow data sampled at the N^{th} probe position	
LiDARData/	Structure array containing flow data sampled with two short-range WindScanner lidars. It only exists if flow measurements with lidars were conducted during the test	
R2D2/	Structure array of flow data measured by the R2D2 lidar	
Position/	Position of the focused laser beam	
x	coordinate x [mm]	250
y	coordinate y [mm]	250
z	coordinate z [mm]	250
vLOS	line-of-sight velocity, v_{LOS} [ms^{-1}]	250
R2D3/	Structure array of flow data measured by the R2D3 lidar	

Continued on next page



Field	Field description [unit of measurements]	f_s [Hz]
Position/	Position of the focused laser beam	
x	coordinate x [mm]	250
y	coordinate y [mm]	250
z	coordinate z [mm]	250
vLOS	line-of-sight velocity, v_{LOS} [ms^{-1}]	250
AvgPosition/	Average position of the R2D2 and R2D3 focused laser beams	
x	coordinate x [mm]	250
y	coordinate y [mm]	250
z	coordinate z [mm]	250
ux	u_x component of the wind speed [ms^{-1}]	250
uy	u_y component of the wind speed [ms^{-1}]	250

630 For signals sampled at frequencies other than 2.5 kHz, the corresponding time histories can be reconstructed by downsampling the time vector to match the signal sampling frequency. Data acquired from the most upstream machine in the cluster are stored in the substructure WT1. For tests involving two or more G1 turbines, data from the central and most downstream machines are stored in the substructures WT2 and WT3, respectively.

4.3 Metadata

635 Each dataset is accompanied by its own test matrix (Fig. 11) that provides a compact, systematic overview of all wind-tunnel experiments included in the corresponding data release. The test matrix is intended as a reference tool to support the interpretation, selection, and comparison of the measurements across different experimental conditions.

Each entry of the test matrix corresponds to a single experimental run and uniquely identifies the associated data file, ensuring a one-to-one correspondence between the experimental metadata and the stored measurement time series. For each test, the matrix documents the execution date and time, the wind-farm layout adopted in the wind tunnel, including the number of G1s and their relative positions within the test section, expressed in the reference frame of Fig. 1. The main characteristics of the inflow conditions reproduced during the experiment are also reported, including the simulated ABL, the turntable angle, the Pitot tube position, and its mean wind speed.

645 The test matrix further specifies the wind-farm control strategy applied in each experiment. This includes the class of control algorithm under investigation and the corresponding control settings assigned to each turbine, such as static or dynamic yaw offsets, power curtailment or derating, amplitude and frequency of the Helix or Pulse control. This information allows controlled cases to be clearly distinguished from baseline (greedy) operation and enables consistent comparisons across different control strategies.

650 For experiments that include dedicated flow measurements, the test matrix indicates the availability of these data and summarizes the associated measurement configurations, including the measurement technique and the location of the flow surveys.

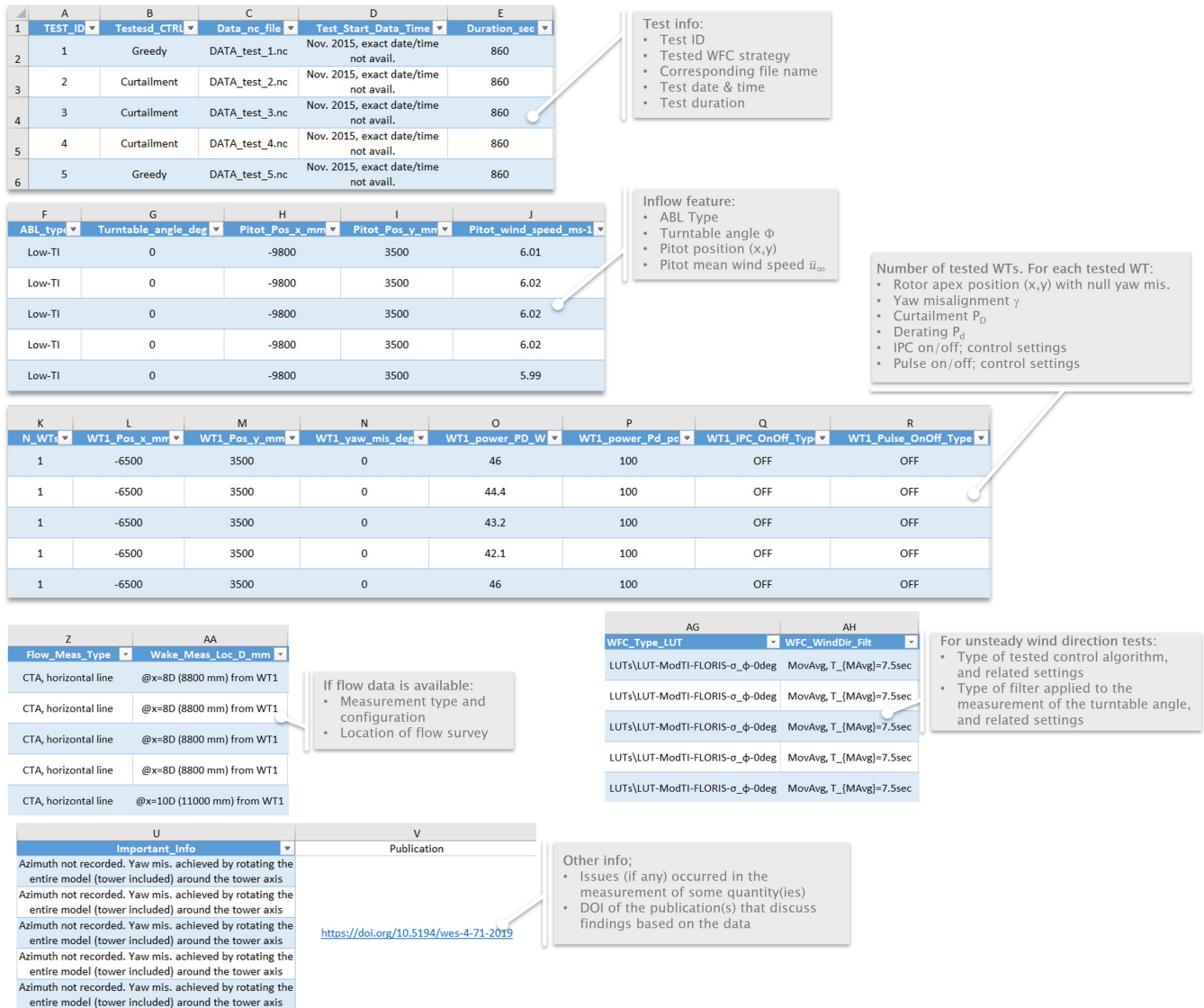


Figure 11. Test matrix summarizing all wind-tunnel experiments included in the corresponding dataset. For each experimental run, the matrix reports: the test identifier, the tested wind-farm control strategy, the execution date and time, the main inflow conditions reproduced in the wind tunnel, the wind-farm layout and turbine positions in the test section, the turbine-level control settings, and the availability and configuration of any dedicated wake measurements. Each entry in the test matrix uniquely identifies the associated data file and provides the reference metadata required to interpret and compare the measurements across different experimental conditions.



This facilitates the identification of test cases suitable for wake-related analyses and the correct interpretation of flow-field data in relation to turbine operating conditions.

For experiments with dynamically changing wind direction, the test matrix reports the applied control algorithm and settings, as well as the filter used to process the measured turntable angle.

655 Finally, the test matrix reports any issues that occurred with one or more sensors during data acquisition, as well as previous publications that present findings derived from the data analysis.

5 Numerical models

The experimental dataset is accompanied by a set of numerical models, listed in Table 4, which simulate different aspects of the G1 wind-tunnel experiments. Two of the provided models focus on the aeroservoelastic behavior of the G1 turbines and do not explicitly resolve the wakes generated in the wind tunnel or their interaction with downstream machines. One of the numerical models, instead, explicitly accounts for wake development and wake-turbine interactions within the wind-tunnel environment. A synthetic representation of the inflow conditions imposed in the wind tunnel, used as input to the numerical simulations, is also provided. Finally, three-dimensional CAD models of the G1 turbine are provided for two configurations: with the standard and with the fast yaw actuator.

Table 4. Overview of the provided numerical models, corresponding software, description, and repository.

Numerical model	Software	Model description	Model repository
3D CAD	-	see Sect. 5.1	https://doi.org/10.5281/zenodo.19047499
Synthetic inflow	SOWFA	see Sect. 5.2	Mod-TI: https://doi.org/10.5281/zenodo.18860646 High-TI: https://doi.org/10.5281/zenodo.19004026
G1 drive-train and tower dynamics	Simulink, v13.38	see Sect. 5.3	https://doi.org/10.5281/zenodo.18755240
G1 aeroservoelasticity	OpenFast, v4.1.2	see Sect. 5.4	https://doi.org/10.5281/zenodo.18772302
Wakes and wake-turbine interaction within the wind tunnel	AMR-Wind, v3.8.0	see Sect. 5.5	https://doi.org/10.5281/zenodo.18874300

665 The numerical models can complement the experimental dataset by predicting physical quantities that were not directly measured during the experiments (e.g., loads, deflections, and accelerations of G1 components, and flow-related quantities), thereby supporting a more comprehensive interpretation of the investigated phenomena. Furthermore, the models provide a framework for assessing innovative control techniques and for validating supporting technologies prior to wind-tunnel testing.

A validation of the models using a subset of the experimental data described in Sect. 4.1 is presented in Appendix A.

670 5.1 Three-dimensional CAD model

The three-dimensional CAD models are simplified representations of the G1 geometry that retain the machine external shape. The provided data (Campagnolo et al., 2026i) consists of two STEP (.stp) files representing the nominal geometry of a G1



turbine characterized by: a collective blade pitch equal to $\beta_{\text{opt}} = 0.42^\circ$, i.e. the fine-pitch of the nominal control trajectory in region II; zero rotor azimuth ($\psi = 0$); zero nacelle yaw angle ($\gamma_{\text{nac}} = 0$).

675 These CAD geometries are suitable for generating conformal meshes for blade-resolved CFD simulations. It should be noted that, owing to manufacturing tolerances in the blade production process, minor discrepancies may exist between the nominal G1 blade geometry and the actual geometry of the tested blades, which is not known.

5.2 Synthetic inflow

680 Time histories of the synthetic inflows generated by two LES analyses, aimed at reproducing the Mod-TI and High-TI atmospheric boundary layers (ABLs), are provided. The simulations were performed using the Simulator fOr Wind Farm Applications (SOWFA, Churchfield et al. (2012)), including an explicit representation of the spires and roughness elements used to generate the boundary layer in the wind tunnel. Further details of the numerical setup are reported in Wang et al. (2019).

685 The provided datasets (Campagnolo et al., 2026k, l) consist of time histories of the three velocity components sampled along a vertical plane located 19.1 m downstream of the inlet, i.e. 10 m upstream of the turntable center, and therefore very close to the location of the corresponding experimental inflow mapping. For the Mod-TI case, the time history spans approximately 70 s, with data sampled at 0.9 ms intervals. For the High-TI case, the time history spans approximately 40 s, with data sampled at 1 ms intervals. For each time instant, a text file is provided in the corresponding folder containing the three instantaneous components of the velocity vector sampled at the mesh nodes. The coordinates of the mesh nodes are specified in a separate file.

690 The synthetic inflow can be scaled following the same procedure suggested for the experimental inflow mapping, described in Sect. 4.1.1. The resulting inflows have been used in several studies (Wang et al., 2017a, 2018b, a, 2019, 2020d, a, c, 2021; Bortolin et al., 2026; Mühle et al., 2026) to numerically assess the impact of a wide range of wind-farm control strategies on the performance of a cluster of G1 turbines and their shed wakes.

5.3 Simulink model

695 A two-degree-of-freedom (2-DOF) numerical model of the G1 turbine is implemented in Simulink. The model neglects blade and drivetrain flexibility and resolves the drivetrain and north-south tower dynamics, the latter represented by a mass-spring-damper system.

700 For aligned operation ($\gamma = 0^\circ$), the rotor aerodynamic power and thrust are computed using Blade Element Momentum (BEM) theory, as implemented in the OpenFAST model described in Sect. 5.4. Specifically, simulations were performed for multiple combinations of wind speed, tip-speed ratio, and collective blade pitch. The resulting aerodynamic power and thrust coefficients are stored in three-dimensional LUTs, which are interpolated in Simulink during model execution.

The model can also predict power and thrust losses induced by yaw misalignment. To this end, the approach proposed in Tamaro et al. (2024) is adopted, which accounts for the effect of yaw misalignment on rotor aerodynamic performance as collective pitch, tip-speed ratio, rotor speed, and vertical shear vary. The corresponding thrust and power loss factors, η_T and



705 η_P , are stored in five-dimensional LUTs and interpolated during model execution. These loss factors are applied to the thrust and power predicted under aligned conditions.

The 2-DOF numerical model includes the controller responsible for tracking the prescribed control trajectory, also during curtailed or derated operation (see Sect. 2.2.6). The temporal evolution of wind speed is defined by the REWS estimated from the appropriately scaled synthetic inflow.

710 The provided model (Campagnolo et al., 2026g) consists of a Simulink file and its parameters, available in a MATLAB (.mat) file. The model has been used, in its original or slightly modified form, to support research on wind-turbine and wind-farm control strategies (Campagnolo et al., 2022a; Tamaro et al., 2026).

5.4 OpenFast model

The aeroservoelastic behavior of the G1 turbine is modeled in OpenFAST (Jonkman et al., 2019) using the following modules:

- 715 – **ElastoDyn (v1.03)**: resolves the structural dynamics of the G1 blades, tower, and drivetrain. The mass and stiffness distributions of the structural components are based on their nominal properties. The first fore-aft and side-side natural frequencies of the tower were tuned using the tower load spectra. Similarly, the drivetrain stiffness was tuned to match the first drivetrain natural frequency inferred from the torque-meter spectra. Higher tower modes and blade natural frequencies may differ from the experimental ones, which are unknown. However, note that the structural design of the blades is driven by strength requirements; as a result, the natural frequencies are much higher and not representative of the frequencies of an aeroelastically-scaled model. Virtual load sensors, placed at the same locations as the G1 load sensors, are also implemented. Finally, two versions of the ElastoDyn input files are provided: one for the standard yaw actuator and the other for the fast yaw actuator.
- 720 – **AeroDyn (v15.03)**: computes aerodynamic loads using a BEM-based formulation with improved performance at large skew angles (Branlard et al., 2024). Airfoil polars were specifically tailored to achieve good agreement between experimental and numerical performance under aligned operating conditions (Wang et al., 2020b).
- 725 – **ServoDyn (v1.05)**: implements all control functionalities described in Sect. 2.2.6, with the exception of the IPC block for load reduction. Specifically, the controller implemented in Simulink is compiled into a Bladed-style Dynamic Link Library (DISCON.dll) following the approach of Mulders et al. (2020), with control parameters (e.g., curtailment, derating, and the amplitude and frequency of wake-mixing techniques) specified in an external file (DISCON.in).
- 730 – **InflowWind (v3.01)**: defines the inflow wind conditions using the appropriately scaled synthetic inflow.

The provided data (Campagnolo et al., 2026h) includes the OpenFAST input files, the 64-bit DISCON.dll, the DISCON.in file containing the control settings, and an example inflow file modelling the Mod-TI ABL. The Simulink model of the controller is also provided, enabling the controller compilation for other operating environments.



735 5.5 AMR-Wind model

A digital twin of the experimental facility is implemented within the open-source, GPU-accelerated flow solver *AMR-Wind* (Sharma et al., 2024; Kuhn et al., 2025), which solves the incompressible Navier-Stokes equations with Boussinesq buoyancy, Coriolis forcing, and actuator forcing. The flow is advanced in time using a fixed time step of $\Delta t = 2.5 \times 10^{-4}$ s, for a total simulated time of 30 s. The computational domain spans $x \in [-10.0, 14.2]$ m, $y \in [-6.92, 6.92]$ m, and $z \in [0.0, 3.84]$ m, and
740 is discretized on a base mesh of $304 \times 176 \times 48$ cells with three adaptive mesh refinement (AMR) levels, resulting in a mesh size of 0.0098 m (equal to $\approx D/112$) at the turbine rotor disk. No-slip wall boundary conditions are imposed on the lateral boundaries (y_{lo} , y_{hi}) and at upper boundary (z_{hi}), while the streamwise boundaries x_{lo} and x_{hi} are modeled as mass inflow at x_{lo} and pressure outflow at x_{hi} . A surface roughness length $z_0 = 10^{-3}$ m is used at the lower boundary (z_{lo}).

Realistic inflow conditions are imposed through ingestion of time-resolved velocity fields from a precursor LES (Mod-TI
745 synthetic inflow, see Sect. 5.2), using the boundary-plane inflow capability of AMR-Wind at x_{lo} . AMR-Wind version v3.8.0 (and AMReX v24.10) was used and minimally modified such that the ingested velocity fields can be scaled by a constant factor to match the experimental wind conditions. The small turbulence scales in the LES are modeled with the AMD subgrid-scale model.

Within the provided datasets (Campagnolo et al., 2026j), each scaled wind turbine is modeled with the Actuator Line Model
750 (ALM) corrected through the vortex-based tip/smearing correction of Meyer Forsting et al. (2019), which couples AMR-Wind with OpenFAST to capture the aeroservoelastic response of each G1 turbine. Each rotor blade is discretized using 60 actuator points and 12 points along the tower, with a Gaussian smearing width $\epsilon = 0.013$ m.

The CFD solver is coupled with OpenFAST v3.5.0. The G1 turbine modelling files and the closed-loop control system are identical to those used in the model described in Sect. 5.4. The controller is interfaced with OpenFAST via a dynamic library
755 compiled on a Linux system.

6 Conclusions

This paper presents a new open-access experimental dataset specifically designed for wind-farm control and wake-interaction research. The dataset comprises time-resolved structural loads, actuator commands, turbine operating states, and wake measurements obtained from wind-tunnel experiments featuring actuated and instrumented scaled wind turbine models. The measurements cover a broad range of wake-control strategies, including yaw-based wake steering, dynamic yaw actuation, Pulse-based
760 wake mixing, Helix control, curtailment and derating strategies, individual pitch control, and combinations thereof.

A key distinguishing feature of the dataset is the simultaneous availability of actuator commands, measured turbine responses, and high-frequency structural load measurements under controlled and repeatable inflow conditions. This enables detailed investigations of controller tracking performance, load variability, and dynamic turbine behaviour induced by active
765 wake-control strategies. In addition to the experimental measurements, the database provides numerical models reproducing the experimental configurations, thereby establishing a reproducible benchmarking framework that supports systematic validation, sensitivity analyses, and model-to-model comparison.



By addressing the current scarcity of publicly available time-resolved datasets tailored to wind-farm control studies, this work contributes to ongoing community efforts aimed at enhancing transparency, reproducibility, and model fidelity in wind-farm control research. The dataset is expected to support validation of control-oriented aeroelastic and wake-interaction models, fatigue-relevant load assessments under active wake-control operation, and benchmarking of numerical tools used for wind-farm design and control.

Future extensions may include additional inflow conditions, further control strategies, and expanded numerical reference cases, with the aim of progressively consolidating this dataset as a community benchmark for controlled wake-interaction studies.

Appendix A: Validation of the numerical models

This section presents a validation of the models described in Sect. 5 against a subset of the experimental data presented in Sect. 4.1. Table A1 lists, for each validated numerical model, the data obtained from the validation simulations, together with the corresponding repository links.

Table A1. Overview of the provided simulation data and corresponding repository

Numerical model	Provided simulation data	Data repository
G1 drive-train and tower dynamics	In. and out. variables, stored in MATLAB (.mat) files	https://doi.org/10.5281/zenodo.18755240
G1 aeroservoelasticity	OpenFast output files (.outb)	https://doi.org/10.5281/zenodo.18772302
Wakes and wake-turbine interaction within the wind tunnel	AMR-Wind (.nc) and OpenFast (.outb) output files	https://doi.org/10.5281/zenodo.18874300

780 A1 Validation of the synthetic inflow

Figure A1 shows a numerical-experimental comparison of the longitudinal turbulence intensity (TI, lower panels) and the mean longitudinal velocity \bar{u}_x (upper panels), with the latter normalized by the corresponding mean velocity at the Pitot tube position $\bar{u}_{x,P}$. Panels a-d and e-h present the comparison for Mod-TI and High-TI inflow conditions, respectively.

The synthetic inflow reproduces reasonably well the variability of both the mean velocity and the longitudinal turbulence intensity, along both the lateral direction (panels a, c, e, g) and the vertical direction (panels b, d, f, h), with errors on the order of a few percentage points. Further comparisons between the turbulent kinetic energy spectra and the autocorrelation of the synthetic inflow and the experimental measurements are reported in Wang et al. (2019).

A2 Validation of the Simulink model

Figure A2 shows a comparison between numerical predictions and experimental data for the most upstream machine in the cluster (WT1), operating under greedy conditions (panels a-d) and under combined yaw misalignment and derating conditions (panels e-h).

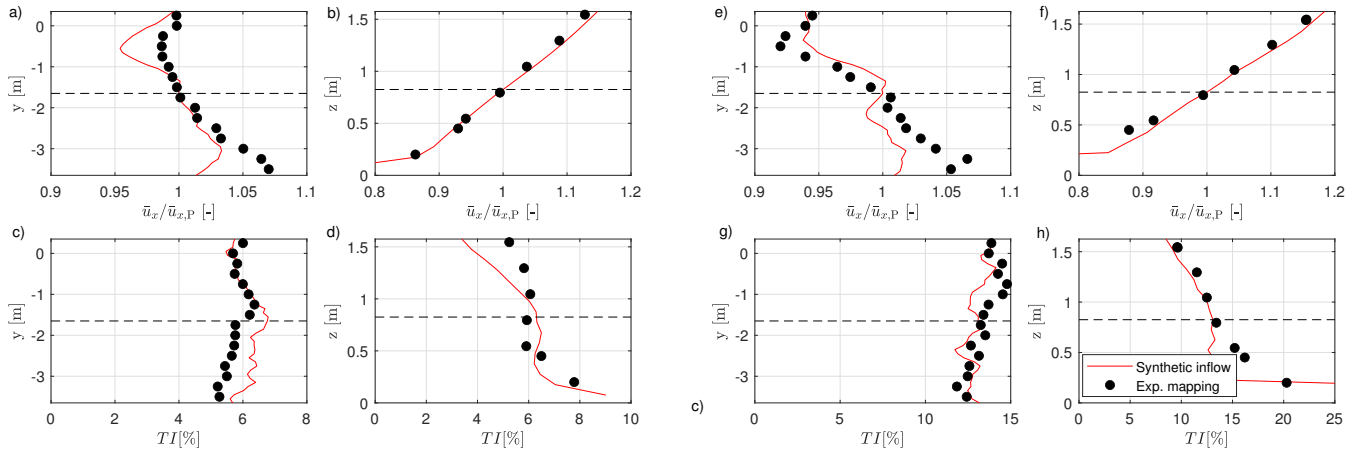


Figure A1. Numerical (red lines) and experimental (black dots) comparison of the longitudinal turbulence intensity (lower panels) and the normalized mean longitudinal velocity (upper panels). Panels a-d and e-h refer to Mod-TI and High-TI inflow conditions, respectively. The black dashed lines mark the Pitot position.

The simulations were performed by reducing the simulated mean wind speed by 0.1 ms^{-1} relative to the mean of the Pitot measurement. These modest adjustments to the simulated ambient conditions, justified by the uncertainty in wind-speed measurements, improve the agreement with the experimental data. The first 5 seconds were also discarded to avoid transient effects in subsequent analyses.

Statistical distributions of the considered quantities are represented using boxplots. For each case, the central line of the box indicates the median value, while the box edges correspond to the first and third quartiles. The whiskers extend to 1.96 times the interquartile range, indicating the variability associated with approximately 95% of the data under the assumption of a normally distributed sample. Outliers are not explicitly shown. The boxplots are positioned and colored to allow direct comparison between experimental and numerical data, as well as between different operating conditions.

The agreement in terms of mean values is very good, except for the blade pitch under combined derating and yaw misalignment. This discrepancy is attributed to the fine-tuning of the optimal pitch implemented in the controller deployed on the G1 turbine (Campagnolo et al., 2023), which differs from the nominal pitch setting implemented in the controller coupled to the simulation environment.

The variability of the considered signals, primarily driven by turbulence in the simulated inflow, is also well captured, except for the tower-base load. This indicates accurate modelling of the drivetrain dynamics in the Simulink environment, whereas the tower motion dynamics is only partially captured by the adopted mass-spring-damper system.

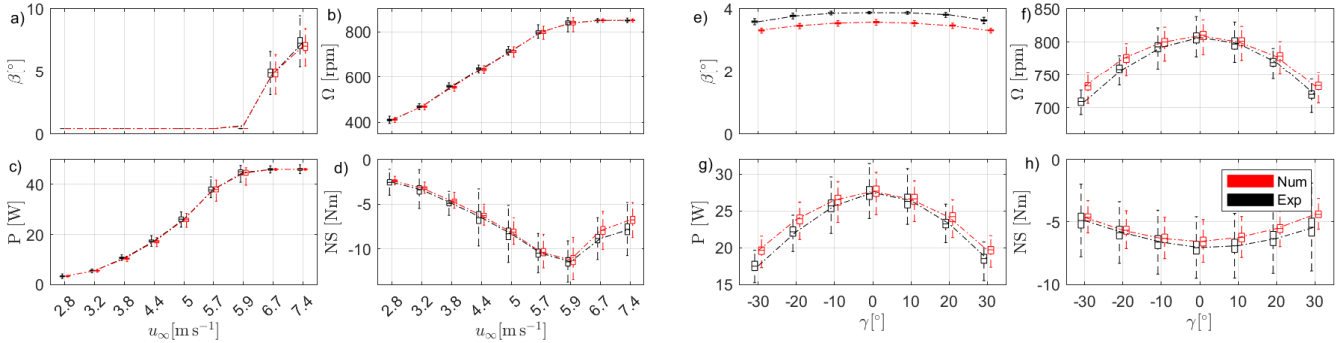


Figure A2. Dataset “Wind turbine data under steady wind direction”. Boxplots **a-d**: comparison between experimental (black) data and numerical (red) predictions for greedy operation of WT1 under Mod-TI inflow conditions and varying wind speed (test IDs: [592:6:640]). Boxplots **e-h**: comparison between experimental (black) data and numerical (red) predictions for derated ($P_d = 0.7$) and yaw-misaligned operation of WT1 under Mod-TI below-rated inflow conditions (test IDs: [667:673]).

A3 Validation of the OpenFast model

Figures A3 and A4 compare numerical predictions with experimental data for WT1 under Helix and DY operation, using
 810 boxplots. The plots illustrate the sensitivity of the main signals measured on the G1 turbine to variations in the amplitude of the investigated mixing strategy, while the mixing frequency is kept constant.

For the simulations performed with Helix, the simulated mean wind speed was reduced by 0.1 ms^{-1} with respect to the mean value measured by the Pitot. The simulations were carried out using the ElastoDyn input files for the fast yaw actuator, with the degree of freedom associated with the first blade edgewise mode disabled, as its activation prevented the solver from
 815 converging. The first 30 seconds were also discarded to avoid transient effects in subsequent analyses. Finally, the numerical loads were corrected for the contributions due to the weight of the tower and the rotor-nacelle assembly at zero yaw, as obtained from a no-wind simulation with the rotor at standstill.

The aeroelastic model accurately captures both the mean values and their variability. In particular, the increase in load variability associated with increasing wake-mixing amplitude is reasonably well reproduced. Only the variability of the side-
 820 side bending moment at the tower base is underestimated by the model.

The spectrum of the numerical side-side bending moment signal shows a marked underestimation of vibrations at frequencies above the first tower mode. This indicates the need to improve the accuracy of the parameters governing high-frequency tower vibrations, which could be achieved through appropriate tuning based on results from a comprehensive experimental modal analysis of the G1 turbine.

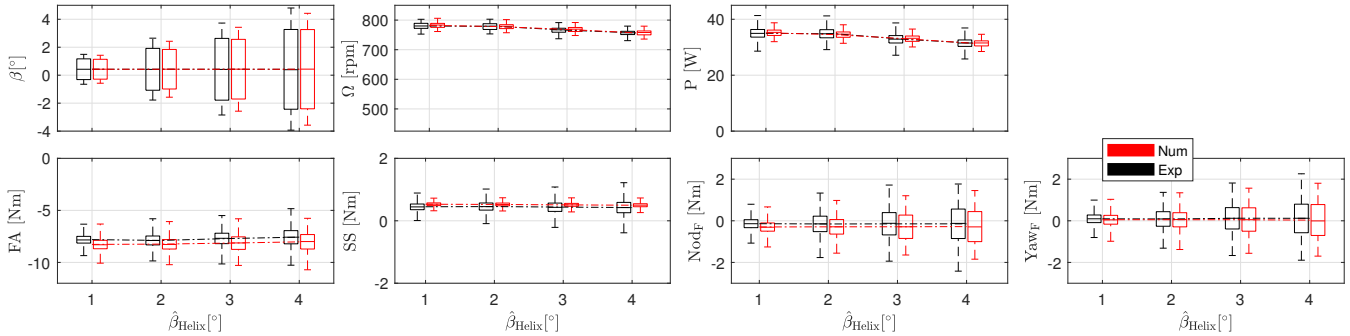


Figure A3. Dataset “Wind turbine data under steady wind direction”. Comparison between experimental (black) data and numerical (red) predictions for CCW Helix operation ($f_{\text{Helix}} = 1.075$) of WT1 under Mod-TI below-rated inflow conditions and varying amplitude $\hat{\beta}_{\text{Helix}}$ (test IDs: [988:991]).

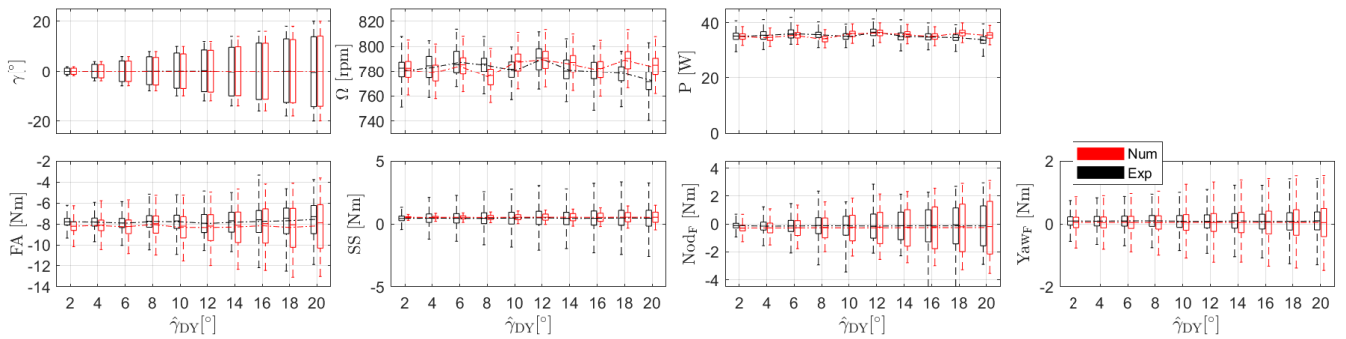


Figure A4. Dataset “Wind turbine data under steady wind direction”. Comparison between experimental (black) data and numerical (red) predictions for DY operation ($f_{\text{DY}} = 0.75$ Hz) of WT1 under Mod-TI below-rated inflow conditions and varying amplitude $\hat{\gamma}_{\text{DY}}$ (test IDs: [1069 1081 1094 1106 1120 1126 1131 1134 1139 1141]).

825 A4 Validation of the AMR-Wind model

Figure A5 shows the average longitudinal velocity field \bar{u}_x predicted by AMR-Wind for two cases of the multiple wake measurement with lidars dataset (see Sect. 4.1.3): greedy control (panel a) and yaw misalignment of the two upstream machines (panel b). The shown data are sampled along a horizontal plane at $z = 0.925$ m, with the wind speed normalized by $\bar{u}_{x,P}$, i.e. the average of the numerical wind speed at the Pitot position.

830 The simulations were performed by suppressing all elastic dofs in OpenFast to simplify the numerical setup. Furthermore, the first ten seconds of simulation data were discarded to remove transient effects.

Figure A6 shows the comparison between the normalized horizontal wake profiles at $z = 0.925$ m measured experimentally with the lidar (black dots) and predicted by AMR-Wind (red lines). The lidar measurements were first filtered using a simple

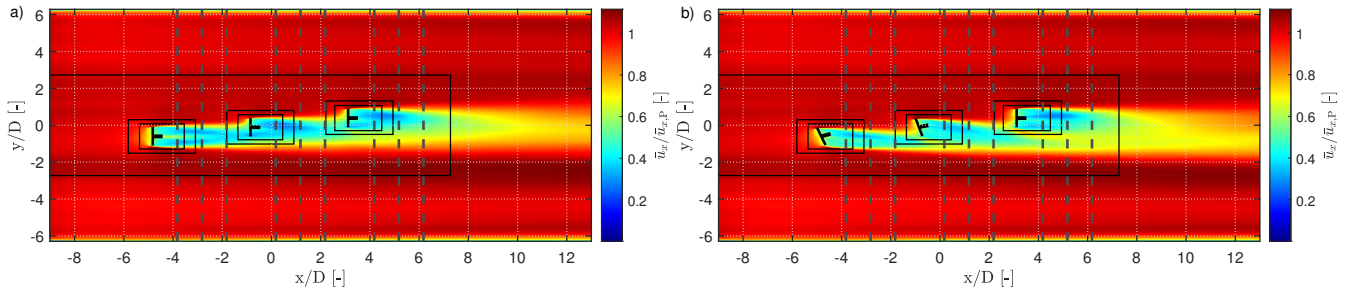


Figure A5. Dataset “Multiple wakes measurement with lidars”. Normalized longitudinal velocity field at $z = 0.925$ m predicted by AMR-Wind for two cases: greedy control (panel **a**, ID 1) and yaw misalignment of the two upstream turbines (panel **b**, ID 4) under Mod-TI below-rated inflow conditions. The black rectangles indicate the three AMR levels. The vertical dashed lines mark the streamwise locations where the comparison between lidar measurements and numerical results is performed (see Fig. A6).

min-max criterion, removing all velocity samples outside the range $0-8 \text{ ms}^{-1}$. Average velocity-deficit profiles were then
835 obtained by binning the data in the x and y directions with bin sizes of 0.05 m and 0.1 m, respectively. The CFD sampling data from AMR-Wind were processed in a similar way. Due to the regular structure of the CFD sampling grid, the data were only binned in the x direction (bin size 0.05 m).

The agreement between numerical and experimental data is very good, with the largest discrepancies observed at 11D for the case when the two upstream turbines are yaw-misaligned.

840 Figure A7 shows the comparison between the power gains $P_{\text{Gain}} = P^{\text{WS}} / P^{\text{Greedy}} - 1$ obtained by yaw-misaligning the two upstream turbines relative to the greedy case, as measured experimentally and predicted numerically. The power losses of WT1 induced by the yaw misalignment are well reproduced by the numerical simulations, whereas the power gains of WT2 and WT3 due to wake steering are slightly overestimated. Overall, the wind-farm power gain almost falls within the expected uncertainty range of the experimental measurements, estimated by propagating the individual sources of error.

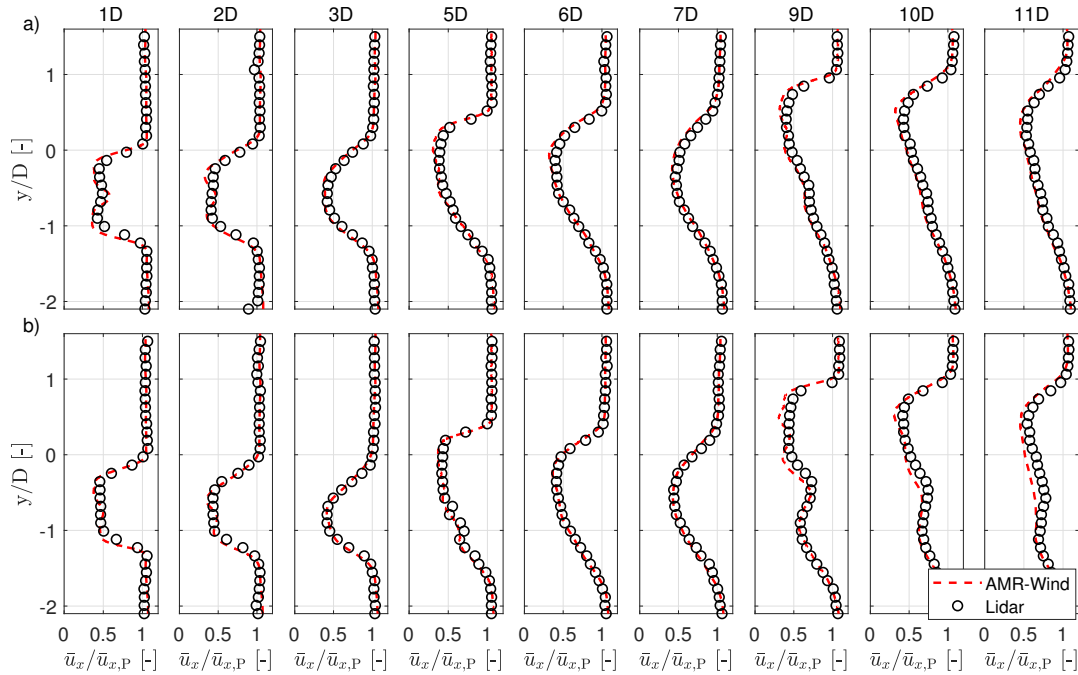


Figure A6. Dataset “Multiple wakes measurement with lidars”. Comparison of experimental lidar data (black dots) and AMR-Wind numerical predictions (red lines) of normalized horizontal wake profiles for greedy control (panel a, ID 1) and yaw misalignment of the two upstream turbines (panel b, ID 4) under Mod-TI below-rated inflow conditions. The comparison is performed at several streamwise locations, expressed in rotor diameters downstream of WT1.

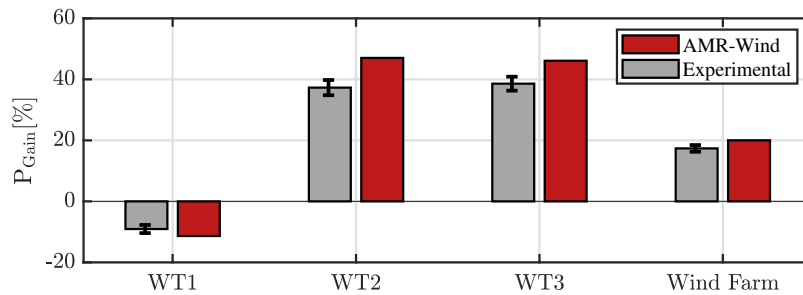


Figure A7. Dataset “Multiple wakes measurement with lidars”. Comparison of experimental measurements and AMR-Wind predictions of the power gain P_{Gain} relative to greedy control (ID 1), obtained by yaw-misaligning the two upstream turbines (ID 4) under Mod-TI below-rated inflow conditions. The error bars represent the uncertainty of the experimental measurements.



845 Appendix: Nomenclature

A	Rotor swept area [m ²]
C_m	Cone coefficient [-]
C_P	Power coefficient [-]
C_T	Thrust coefficient [-]
D	Rotor diameter [m]
EW	East-West tower base bending moment [Nm]
FA	Fore-Aft tower base bending moment [Nm]
f	Frequency [Hz]
f_r	Rotor rotational frequency [Hz]
$K_{Q,I}$	Integral gain of the PI torque controller [Nms]
$K_{Q,P}$	Proportional gain of the PI torque controller [Nm]
$K_{\beta,I}$	Integral gain of the PI pitch controller [-]
$K_{\beta,P}$	Proportional gains of the PI pitch controller [s]
$M_{x,S}, M_{y,S}$	Shaft rotating bending moments [Nm]
Nod_F	Fixed-frame nacelle nodding moment [Nm]
NS	North-South tower base bending moment [Nm]
P	Mechanical power [W]
P_D	Demanded curtailed power [W]
P_d	Power derating factor [-]
P_n	Normalized mechanical power [-]
p_{dyn}	Pitot dynamic pressure [Pa]
Q	Mechanical torque [Nm]
R	Rotor radius [m]
SS	Side-Side tower base bending moment [Nm]
t	Time [s]
T	Rotor thrust force [N]
u_∞	Freestream wind speed [ms ⁻¹]
u_x, u_y, u_z	Velocity components [ms ⁻¹]
v_{LOS}	Line-of-sight velocity measured by lidar [ms ⁻¹]
x, y, z	Longitudinal, lateral, and vertical coordinates [m]
Yaw_F	Fixed-frame nacelle yawing moment [Nm]
z_H	Hub height [m]
z_{SG}	Distance between the rotor apex and the tower strain-gauge section [m]



β_i	Pitch angle of blade i [°]
ϵ_Ω	Rotor speed error [rpm]
γ	Yaw misalignment angle [°]
γ_{nac}	Nacelle yaw angle [°]
$\gamma_{\mathbf{u}}$	Yaw angle of velocity vector [°]
Φ	Turntable angle [°]
$\varphi_{\mathbf{u}}$	Tilt angle of velocity vector [°]
λ	Tip-speed ratio [-]
ρ	Air density [kg m^{-3}]
Ω	Rotor angular velocity [rpm]
ψ	Rotor azimuth angle [°]

$(\cdot)_{\text{Dem}}$	Demanded value
$(\cdot)_{\text{Meas}}$	Measured value
$(\cdot)_{\text{opt}}$	Optimal value
$(\cdot)_{\text{P}}$	Pitot probe reference position
$(\cdot)_{\text{R}}$	Rated value
$(\cdot)_{\text{S}}$	Rotating shaft reference frame

ABL	Atmospheric boundary layer
APC	Active power control
CAD	Computer-aided design
CTA	Constant temperature anemometer
DEL	Damage equivalent load
DIC	Dynamic induction control
DY	Dynamic yaw
IPC	Individual pitch control
LES	Large eddy simulation
PLC	Programmable logic controller
REWS	Rotor effective wind speed
TSR	Tip-speed ratio

850 *Code and data availability.* The "Experimental inflow mapping" dataset (Campagnolo et al., 2026f) is available on Zenodo at <https://doi.org/10.5281/zenodo.18749773> and on WindLab at <https://windlab.hlr.de/dataset/18749773>.



The "Single wake measurement" dataset (Campagnolo et al., 2026c) is available on Zenodo at <https://doi.org/10.5281/zenodo.18732794> and on WindLab at <https://windlab.hlrs.de/dataset/18732794>.

855 The "Double wakes measurement" dataset (Campagnolo et al., 2026e) is available on Zenodo at <https://doi.org/10.5281/zenodo.18743973> and on WindLab at <https://windlab.hlrs.de/dataset/18743973>.

The "Multiple wakes measurement" dataset (Campagnolo et al., 2026b) is available on Zenodo at <https://doi.org/10.5281/zenodo.18731994> and on WindLab at <https://windlab.hlrs.de/dataset/18731994>.

The "Wind turbine data under steady wind direction" dataset (Campagnolo et al., 2026a) is available on Zenodo at <https://doi.org/10.5281/zenodo.18723855> and on WindLab at <https://windlab.hlrs.de/dataset/18723855>.

860 The "Wind turbine data under dynamically varying wind direction" dataset (Campagnolo et al., 2026d) is available on Zenodo at <https://doi.org/10.5281/zenodo.18743431> and on WindLab at <https://windlab.hlrs.de/dataset/18743431>.

The 3D CAD models (Campagnolo et al., 2026i) are available on Zenodo at <https://doi.org/10.5281/zenodo.19047499> and on WindLab at <https://windlab.hlrs.de/dataset/19047499>.

865 The synthetic inflows (Campagnolo et al., 2026k, l) are available on Zenodo at <https://doi.org/10.5281/zenodo.18860646> and <https://doi.org/10.5281/zenodo.19004026>, as well as WindLab at <https://windlab.hlrs.de/dataset/18860646> and <https://windlab.hlrs.de/dataset/19004026>.

The 2-DOF Simulink model and its input/output files for selected cases (Campagnolo et al., 2026g) are available on Zenodo at <https://doi.org/10.5281/zenodo.18755240> and on WindLab at <https://windlab.hlrs.de/dataset/18755240>.

The OpenFast model and its output files for selected cases (Campagnolo et al., 2026h) are available on Zenodo at <https://doi.org/10.5281/zenodo.18772302> and on WindLab at <https://windlab.hlrs.de/dataset/18772302>.

870 The AMR-Wind model and its input/output files for selected cases (Campagnolo et al., 2026j) are available on Zenodo at <https://doi.org/10.5281/zenodo.18874300> and on WindLab at <https://windlab.hlrs.de/dataset/18874300>.

Author contributions. CLB conceived the G1 research concept as a platform for wake behaviour and wind farm control studies, initiated and led the research projects enabling its development and testing, designed and supervised the experimental activities. He contributed to the analysis and interpretation of the results and helped define the overall research direction. FC designed and developed the G1 wind turbines and their acquisition and control systems, covering both system-level definition and detailed engineering, including hardware selection, mechanical design, and control software implementation. He co-designed the experimental campaigns, played a key role in their execution, contributed to data analysis and interpretation, and created and structured the dataset. He led the development of the digital twins of the experimental facility described in the paper. CLB conceived this data description paper, with the initial draft written by FC. FVM, ST, and DB contributed to the design and execution of the experimental activities, data analysis, and technical discussions. AD contributed to the development of the numerical models and the controllers integrated within them. All authors contributed ideas, suggestions, and improvements to the writing and editing of the paper.

Financial support. This work has been supported in part by the German Federal Ministry for Economic Affairs and Energy through projects CompactWind (FKZ: 0325492), e-TWINS (FKZ: 03EI6020A), PowerTracker (FKZ: 03EE2036A), and LifeOdometer (FKZ: 03EE3037B). This work has also been partially supported by the European Union's Horizon Europe Programme through projects CL-WINDCON (grant agreement No. 727477), TWEET-IE (grant agreement No. 101079125), and MERIDIONAL (grant agreement No. 101084216).



Competing interests. At least one of the (co-)authors is a member of the editorial board of *Wind Energy Science*.

Acknowledgements. The authors gratefully acknowledge Insu Paek of Kangwon National University for developing the very first version of the Simulink controller that tracks the regulation trajectory. Emmanouil Nanos, Vlaho Petrović, Manu Prosser, Johannes Schreiber, Chengyu Wang, and Robin Weber from the Technical University of Munich are gratefully acknowledged for their valuable contribution to the development of the G1 model, the execution of the wind-tunnel experiments, the development of the synthetic inflow, and the implementation of the numerical setup in AMR-Wind.

The authors thank Stefano Cacciola, Gabriele Campanardi, Alessandro Croce, Stefano Giappino, Donato Grassi, Luca Ronchi, Paolo Schito, and Alberto Zasso from Politecnico di Milano for conducting the hot-wire flow measurements and for their support during the wind-tunnel experimental campaigns.

The authors also express their gratitude to the Leibniz Supercomputing Centre (LRZ) for providing access and computing time on the SuperMUC Petascale System under Projekt-ID pn67qi “Large-eddy Simulation of wind farm Control beyond Power maximization” (LESCoP).



References

- Bachmann electronic GmbH: System overview, <https://www.bachmann.info/en/system-overview>, last accessed: 2025-12-12, 2025.
- Boorsma, K. and Schepers, J.: New MEXICO experiment. Preliminary Overview with Initial Validation, Tech. Rep. ECN-E-14-048, Energy Research Centre of the Netherlands (ECN), 2014.
- Boorsma, K. and Schepers, J. G.: Rotor experiments in controlled conditions continued: New Mexico, *Journal of Physics: Conference Series*, 753, 022004, <https://doi.org/10.1088/1742-6596/753/2/022004>, 2016.
- Bortolin, D., Tamaro, S., Campagnolo, F., Mühle, F. V., Manolesos, M., Croce, C., and Bottasso, C. L.: An experimental investigation on wake mixing and steering techniques, in: *Journal of Physics: Conference Series*, in review, IOP Publishing, 2026.
- Bortolotti, P., Tarres, H. C., Dykes, K., Merz, K., Sethuraman, L., Verelst, D., and Zahle, F.: IEA Wind TCP Task 37: Systems engineering in wind energy-WP2. 1 Reference wind turbines, <https://doi.org/10.2172/1529216>, 2019.
- Bossanyi, E. A.: Wind turbine control for load reduction, *Wind Energy*, 6, 229–244, <https://doi.org/10.1002/we.95>, 2003.
- Bottasso, C. L. and Campagnolo, F.: Wind tunnel testing of wind turbines and farms, *Handbook of Wind Energy Aerodynamics*, pp. 1077–1126, https://doi.org/10.1007/978-3-030-31307-4_54, 2022.
- Bottasso, C. L., Cacciola, S., and Schreiber, J.: Local wind speed estimation, with application to wake impingement detection, *Renewable Energy*, 116, 155–168, <https://doi.org/10.1016/j.renene.2017.09.044>, 2018.
- Branlard, E., Jonkman, J., Lee, B., Jonkman, B., Singh, M., Mayda, E., and Dixon, K.: Improvements to the blade element momentum formulation of openfast for skewed inflows, in: *Journal of Physics: Conference Series*, vol. 2767, p. 022003, IOP Publishing, <https://doi.org/10.1088/1742-6596/2767/2/022003>, 2024.
- Campagnolo, F.: Wind tunnel testing of scaled wind turbine models: aerodynamics and beyond, 2013.
- Campagnolo, F. and Bottasso, C. L.: On the effectiveness of one-sided wake steering-A wind tunnel study with dynamic direction changes, in: 2021 American Control Conference (ACC), pp. 3070–3075, IEEE, <https://doi.org/10.23919/ACC50511.2021.9483266>, 2021.
- Campagnolo, F., Petrović, V., Schreiber, J., Nanos, E. M., Croce, A., and Bottasso, C. L.: Wind tunnel testing of a closed-loop wake deflection controller for wind farm power maximization, in: *Journal of Physics: Conference Series*, vol. 753, p. 032006, IOP Publishing, <https://doi.org/10.1088/1742-6596/753/3/032006>, 2016.
- Campagnolo, F., Schreiber, J., Garcia, A. M., and Bottasso, C. L.: Wind tunnel validation of a wind observer for wind farm control, in: ISOPE International Ocean and Polar Engineering Conference, pp. ISOPE–I, ISOPE, 2017.
- Campagnolo, F., Molder, A., Schreiber, J., and Bottasso, C. L.: Comparison of analytical wake models with wind tunnel data, in: *Journal of physics: conference series*, vol. 1256, p. 012006, IOP Publishing, <https://doi.org/10.1088/1742-6596/1256/1/012006>, 2019.
- Campagnolo, F., Schreiber, J., and Bottasso, C. L.: Wake deflection control with wind direction changes: Wind tunnel comparison of different wind farm flow models, in: 2020 American Control Conference (ACC), pp. 4817–4823, IEEE, <https://doi.org/10.23919/ACC45564.2020.9147449>, 2020a.
- Campagnolo, F., Weber, R., Schreiber, J., and Bottasso, C. L.: Wind tunnel testing of wake steering with dynamic wind direction changes, *Wind Energy Science*, 5, 1273–1295, <https://doi.org/10.5194/wes-5-1273-2020>, 2020b.
- Campagnolo, F., Castellani, F., Natili, F., Astolfi, D., and Mühle, F.: Wind Tunnel Testing of Yaw by Individual Pitch Control Applied to Wake Steering, *Frontiers in Energy Research*, 10, <https://doi.org/10.3389/fenrg.2022.883889>, 2022a.
- Campagnolo, F., Imširović, L., Braunbehrens, R., and Bottasso, C. L.: Further calibration and validation of FLORIS with wind tunnel data, in: *Journal of Physics: Conference Series*, vol. 2265, p. 022019, IOP Publishing, <https://doi.org/10.1088/1742-6596/2265/2/022019>, 2022b.



- Campagnolo, F., Tamaro, S., Mühle, F., and Bottasso, C. L.: Wind Tunnel Testing of Combined Derating and Wake Steering, *IFAC-PapersOnLine*, 56, 8400–8405, <https://doi.org/10.1016/j.ifacol.2023.10.1034>, 2023.
- 935 Campagnolo, F., Aktan, H. D., Bortolin, D., Tamaro, S., Mühle, F. V., and Bottasso, C. L.: Wind Tunnel Benchmark Dataset for Wind Farm Control Strategies on a Three-Turbine Farm, *Zenodo* [data set], <https://doi.org/10.5281/zenodo.18723855>, 2026a.
- Campagnolo, F., Aktan, H. D., Bortolin, D., Tamaro, S., Mühle, F. V., and Bottasso, C. L.: Wind Tunnel Experimental Dataset for Wind Farm Control with Scanning Lidar Wake Measurements, *Zenodo* [data set], <https://doi.org/10.5281/zenodo.18731994>, 2026b.
- 940 Campagnolo, F., Aktan, H. D., Bortolin, D., Tamaro, S., Mühle, F. V., and Bottasso, C. L.: Wind Tunnel Single-Wake Dataset with Multi-Probe Flow Measurements and Turbine Loads, *Zenodo* [data set], <https://doi.org/10.5281/zenodo.18732794>, 2026c.
- Campagnolo, F., Aktan, H. D., Bortolin, D., Tamaro, S., Mühle, F. V., and Bottasso, C. L.: Wind Tunnel Dataset of Wind Farm Power Boosting and Active Power Control under Unsteady Wind Direction (Three-Turbine Farm), *Zenodo* [data set], <https://doi.org/10.5281/zenodo.18743431>, 2026d.
- 945 Campagnolo, F., Aktan, H. D., Bortolin, D., Tamaro, S., Mühle, F. V., and Bottasso, C. L.: Wind Tunnel Double-Wake Dataset with Multi-Probe Three-Component Velocity Measurements (NetCDF Collection), *Zenodo* [data set], <https://doi.org/10.5281/zenodo.18743973>, 2026e.
- Campagnolo, F., Aktan, H. D., Bortolin, D., Tamaro, S., Mühle, F. V., and Bottasso, C. L.: Wind Tunnel Atmospheric Boundary Layer Inflow Dataset (Lidar & Hot-Wire Measurements), *Zenodo* [data set], <https://doi.org/10.5281/zenodo.18749773>, 2026f.
- 950 Campagnolo, F., Aktan, H. D., and Bottasso, C. L.: Simulink 2-DOF Model of the G1 Wind Turbine with Simulation Inputs and Outputs for Wind Farm Control Benchmarking, *Zenodo* [numerical model and data set], <https://doi.org/10.5281/zenodo.18755240>, 2026g.
- Campagnolo, F., Aktan, H. D., and Bottasso, C. L.: OpenFAST G1 Model and Validation Simulations for the Wind Tunnel Benchmark Dataset for Wind Farm Control Strategies, *Zenodo* [numerical model and data set], <https://doi.org/10.5281/zenodo.18772302>, 2026h.
- Campagnolo, F., Bortolin, D., and Bottasso, C. L.: Simplified CAD geometry of the G1 wind turbine for blade-resolved CFD simulations, *Zenodo* [numerical model], <https://doi.org/10.5281/zenodo.19047499>, 2026i.
- 955 Campagnolo, F., Bortolin, D., Prosser, M., Tamaro, S., and Bottasso, C. L.: Dataset for the AMR-Wind digital-twin simulations of the three-turbine experimental facility, *Zenodo* [numerical model and data set], <https://doi.org/10.5281/zenodo.18874300>, 2026j.
- Campagnolo, F., Tamaro, S., and Bottasso, C. L.: Mod-TI Synthetic Inflow Dataset for the G1 Wind Farm Control Benchmark, *Zenodo* [data set], <https://doi.org/10.5281/zenodo.18860646>, 2026k.
- 960 Campagnolo, F., Tamaro, S., and Bottasso, C. L.: High-TI Synthetic Inflow Dataset for the G1 Wind Farm Control Benchmark, *Zenodo* [data set], <https://doi.org/10.5281/zenodo.19004026>, 2026l.
- Cermak, J. E.: Wind-tunnel development and trends in applications to civil engineering, *Journal of Wind Engineering and Industrial Aerodynamics*, 91, 355–370, [https://doi.org/10.1016/S0167-6105\(02\)00396-3](https://doi.org/10.1016/S0167-6105(02)00396-3), 2003.
- Churchfield, M., Lee, S., Moriarty, P., Martinez, L., Leonardi, S., Vijayakumar, G., and Brasseur, J.: A large-eddy simulation of wind-plant aerodynamics, in: 50th AIAA aerospace sciences meeting including the new horizons forum and aerospace exposition, p. 537, 2012.
- 965 Croce, A., Cacciola, S., and Isella, F.: Combining wake redirection and derating strategies in a load-constrained wind farm power maximization, *Wind Energy Science*, 9, 1211–1227, <https://doi.org/10.5194/wes-9-1211-2024>, 2024.
- Davis, R. S.: Equation for the Determination of the Density of Moist Air (1981/91), *Metrologia*, 29, 67–70, <https://doi.org/10.1088/0026-1394/29/1/008>, 1992.
- 970 Diana, G., De Ponte, S., Falco, M., and Zasso, A.: A new large wind tunnel for civil-environmental and aeronautical applications, *Journal of Wind Engineering and Industrial Aerodynamics*, 74, 553–565, [https://doi.org/10.1016/S0167-6105\(98\)00050-6](https://doi.org/10.1016/S0167-6105(98)00050-6), 1998.



- Doekemeijer, B. M., Kern, S., Maturu, S., Kanev, S., Salbert, B., Schreiber, J., Campagnolo, F., Bottasso, C. L., Schuler, S., Wilts, F., et al.: Field experiment for open-loop yaw-based wake steering at a commercial onshore wind farm in Italy, *Wind Energy Science*, 6, 159–176, <https://doi.org/10.5194/wes-6-159-2021>, 2021.
- 975 Draper, M., Guggeri, A., López, B., Díaz, A., Campagnolo, F., and Usera, G.: A Large Eddy Simulation framework to assess wind farm power maximization strategies: Validation of maximization by yawing, in: *Journal of Physics: Conference Series*, vol. 1037, p. 072051, IOP Publishing, <https://doi.org/10.1088/1742-6596/1037/7/072051>, 2018a.
- Draper, M., Guggeri, A., Mendina, M., Usera, G., and Campagnolo, F.: A large eddy simulation-actuator line model framework to simulate a scaled wind energy facility and its application, *Journal of Wind Engineering and Industrial Aerodynamics*, 182, 146–159, <https://doi.org/10.1016/j.jweia.2018.09.010>, 2018b.
- 980 Fleming, P., King, J., Dykes, K., Simley, E., Roadman, J., Scholbrock, A., Murphy, P., Lundquist, J. K., Moriarty, P., Fleming, K., et al.: Initial results from a field campaign of wake steering applied at a commercial wind farm—Part 1, *Wind Energy Science*, 4, 273–285, <https://doi.org/10.5194/wes-4-273-2019>, 2019.
- Fleming, P., King, J., Simley, E., Roadman, J., Scholbrock, A., Murphy, P., Lundquist, J. K., Moriarty, P., Fleming, K., van Dam, J., et al.: Continued results from a field campaign of wake steering applied at a commercial wind farm: Part 2, *Wind Energy Science*, 5, 945–958, <https://doi.org/10.5194/wes-5-945-2020>, 2020.
- 985 Fontanella, A., Fusetti, A., Cioni, S., Papi, F., Muggiasca, S., Persico, G., Dossena, V., Bianchini, A., and Belloli, M.: Wake development in floating wind turbines: new insights and an open dataset from wind tunnel experiments, *Wind Energy Science*, 10, 1369–1387, <https://doi.org/10.5194/wes-10-1369-2025>, 2025.
- 990 Frederik, J. A., Doekemeijer, B. M., Mulders, S. P., and van Wingerden, J.-W.: The helix approach: Using dynamic individual pitch control to enhance wake mixing in wind farms, *Wind Energy*, 23, 1739–1751, <https://doi.org/10.1002/we.2513>, 2020a.
- Frederik, J. A., Weber, R., Cacciola, S., Campagnolo, F., Croce, A., Bottasso, C., and van Wingerden, J.-W.: Periodic dynamic induction control of wind farms: proving the potential in simulations and wind tunnel experiments, *Wind Energy Science*, 5, 245–257, <https://doi.org/10.5194/wes-5-245-2020>, 2020b.
- 995 Frederik, J. A., Simley, E., Brown, K. A., Yalla, G. R., Cheung, L. C., and Fleming, P. A.: Comparison of wind farm control strategies under realistic offshore wind conditions: turbine quantities of interest, *Wind Energy Science*, 10, 755–777, <https://doi.org/10.5194/wes-10-755-2025>, 2025.
- Hand, M. M., Simms, D. A., Fingersh, L. J., Jager, D. W., Cotrell, J. R., Schreck, S., and Larwood, S. M.: Unsteady Aerodynamics Experiment Phase VI: Wind Tunnel Test Configurations and Available Data Campaigns, Tech. Rep. NREL/TP-500-29955, National Renewable Energy Laboratory (NREL), Golden, CO, USA, 2001.
- 1000 Holmes, J. D.: *Wind Loading of Structures*, CRC Press, 3rd edn., <https://doi.org/10.1201/b18029>, 2015.
- Ishihara, T. and Zhou, T.: Wind tunnel measurement dataset of turbulent flow over two-dimensional ridges and three-dimensional hills with smooth and rough surfaces, *Data in Brief*, p. 112260, <https://doi.org/10.1016/j.dib.2025.112260>, 2025.
- ISO, I. and OIML, B.: *Guide to the Expression of Uncertainty in Measurement*, Aenor Madrid, Spain, 1993.
- 1005 Jonkman, J. M., Sprague, M. A., and Jonkman, B. J.: OpenFAST: An Open-Source Tool for Wind Turbine Simulation, Tech. Rep. NREL/TP-5000-74917, National Renewable Energy Laboratory (NREL), Golden, CO, USA, <https://openfast.readthedocs.io>, 2019.
- Juangarcia, D. A., Eguinoa, I., and Knudsen, T.: Derating a single wind farm turbine for reducing its wake and fatigue, in: *Journal of Physics: Conference Series*, vol. 1037, p. 032039, IOP Publishing, <https://doi.org/10.1088/1742-6596/1037/3/032039>, 2018.
- Kareem, A.: Bluff body aerodynamics and aeroelasticity: a wind effects perspective, *Journal of wind and Engineering*, 7, 30–74, 2010.



- 1010 Kim, H., Kim, K., Bottasso, C. L., Campagnolo, F., and Paek, I.: Wind turbine wake characterization for improvement of the Ainslie eddy viscosity wake model, *Energies*, 11, 2823, <https://doi.org/10.3390/en11102823>, 2018.
- Kuhn, M. B., Henry de Frahan, M. T., Mohan, P., Deskos, G., Churchfield, M., Cheung, L., Sharma, A., Almgren, A., Ananthan, S., Brazell, M. J., A., M. L., Thedin, R., Rood, J., Sakievich, P., Vijayakumar, G., Zhang, W., and Sprague, M. A.: AMR-Wind: A performance-portable, high-fidelity flow solver for wind farm simulations, *Wind Energy*, 28, –, <https://doi.org/10.1002/we.70010>, 2025.
- 1015 Laffin, K., Brodersen, O., Rakowitz, M., Vassberg, J., Wahls, R., Morrison, J., Tinoco, E., and Godard, J.-L.: Summary of data from the second AIAA CFD drag prediction workshop, in: 42nd AIAA Aerospace Sciences Meeting and Exhibit, p. 555, <https://doi.org/10.2514/6.2004-555>, 2004.
- Levy, D., Wahls, R., Zickuhr, T., Vassberg, J., Agrawal, S., Pirzadeh, S., and Hensch, M.: Summary of data from the first AIAA CFD drag prediction workshop, in: 40th AIAA Aerospace Sciences Meeting & Exhibit, p. 841, <https://doi.org/10.2514/6.2002-841>, 2002.
- 1020 Levy, D., Laffin, K., Vassberg, J., Tinoco, E., Mani, M., Rider, B., Brodersen, O., Crippa, S., Rumsey, C., Wahls, R., et al.: Summary of data from the fifth AIAA CFD drag prediction workshop, in: 51st AIAA Aerospace Sciences Meeting including the New Horizons Forum and Aerospace Exposition, p. 46, <https://doi.org/10.2514/6.2013-46>, 2013.
- Lio, W. H., Mirzaei, M., and Larsen, G. C.: On wind turbine down-regulation control strategies and rotor speed set-point, in: *Journal of Physics: Conference Series*, vol. 1037, p. 032040, IOP Publishing, <https://doi.org/10.1088/1742-6596/1037/3/032040>, 2018.
- 1025 Madsen, H., Fuglsang, P., Romblad, J., Enevoldsen, P., Laursen, J., Jensen, L., Bak, C., Paulsen, U. S., Gaunna, M., Sorensen, N. N., et al.: The dan-aero mw experiments, in: 48th Aiaa Aerospace Sciences Meeting Including the New Horizons Forum and Aerospace Exposition, p. 645, <https://doi.org/10.2514/6.2010-645>, 2010.
- Maxon Motor AG: Maxon motor datasheet, <https://www.maxongroup.com>, last accessed: 2026-01-05, 2026.
- Meyer Forsting, A. R., Pirrung, G. R., and Ramos-García, N.: A vortex-based tip/smearing correction for the actuator line, *Wind Energy Science*, 4, 369–383, <https://doi.org/10.5194/wes-4-369-2019>, 2019.
- 1030 Mikkelsen, T., {Siggaard Knudsen}, S., Sjöholm, M., Angelou, N., and Pedersen, A.: WindScanner.eu - a new Remote Sensing Research Infrastructure for On- and Offshore Wind Energy, in: *Proceedings of the International Conference on Wind Energy: Materials, Engineering, and Policies (WEMEP-2012)*, 2012.
- Miner, M. A.: Cumulative damage in fatigue, <https://doi.org/10.1115/1.4009458>, 1945.
- 1035 Moriarty, P., Hamilton, N., Debnath, M., Herges, T., Isom, B., Lundquist, J. K., Maniaci, D., Naughton, B., Pauly, R., Roadman, J., Shaw, W., van Dam, J., and Wharton, S.: American WAKE experimeNt (AWAKEN), Tech. Rep. NREL/TP-5000-75789, National Renewable Energy Laboratory (NREL), Golden, CO, USA, 2020.
- Mühle, F. V., Campagnolo, F., Llobell Buigues, J., and Bottasso, C. L.: Design and testing of a model-scale yaw mechanism for an experimental wind turbine model, *Journal of Physics: Conference Series*, 2265, 022094, <https://doi.org/10.1088/1742-6596/2265/2/022094>, 2022.
- 1040 Mühle, F. V., Heckmeier, F. M., Campagnolo, F., and Breitsamter, C.: Wind tunnel investigations of an individual pitch control strategy for wind farm power optimization, *Wind Energy Science*, 9, 1251–1271, <https://doi.org/10.5194/wes-9-1251-2024>, 2024.
- Mühle, F. V., Tamaro, S., Bortolin, D., Campagnolo, F., and Bottasso, C. L.: Wake mixing wind farm control with synchronized dynamic yaw for power optimization, in: *Journal of Physics: Conference Series*, in review, IOP Publishing, 2026.
- 1045 Mulders, S. P., Zaaier, M. B., Bos, R., and van Wingerden, J.-W.: Wind turbine control: Open-source software for control education, standardization and compilation, *Journal of Physics: Conference Series*, 1452, 012010, <https://doi.org/10.1088/1742-6596/1452/1/012010>, 2020.



- Nam, Y.: Wind Turbine System Control, GS intervention, pp. 430–441, 2013.
- National Instruments: PXI Platform, <https://www.ni.com/en/shop/pxi.html>, last accessed: 2025-12-12, 2024.
- 1050 Petrović, V. and Campagnolo, F.: Experimental validation of wind turbine higher harmonic control using shaft loads measurements, in: 2013 European Control Conference (ECC), pp. 472–477, IEEE, <https://doi.org/10.23919/ECC.2013.6669709>, 2013.
- Politecnico di Milano: Aerodynamic Laboratory, <https://www.aero.polimi.it/en/experimental-labs/aerodynamic-laboratory>, last accessed: 2025-12-12, 2025.
- Raffel, M., De Gregorio, F., de Groot, K., Schneider, O., Sheng, W., Gibertini, G., and Seraudie, A.: On the generation of a helicopter
1055 aerodynamic database, *The Aeronautical Journal*, 115, 103–112, <https://doi.org/10.1017/S0001924000005492>, 2011.
- Rivers, M. B. and Dittberner, A.: Experimental investigations of the NASA common research model, *Journal of Aircraft*, 51, 1183–1193, <https://doi.org/10.2514/1.C032626>, 2014.
- Ruisi, R. and Bossanyi, E.: Engineering models for turbine wake velocity deficit and wake deflection. A new proposed approach for onshore and offshore applications, *Journal of Physics: Conference Series*, 1222, 012 004, <https://doi.org/10.1088/1742-6596/1222/1/012004>, 2019.
- 1060 Schepers, J. G., Boorsma, K., Cho, T., Gomez-Iradi, S., Schaffarczyk, P., Jeromin, A., Lutz, T., Meister, K., Stoevesandt, B., Schreck, S., et al.: Final report of IEA task 29, Mexnet (phase 1): analysis of Mexico wind tunnel measurements, Tech. Rep. ECN-E–12-004, Energy Research Centre of the Netherlands (ECN), 2012.
- Schepers, J. G., Boorsma, K., and Munduate, X.: Final Results from Mexnext-I: Analysis of detailed aerodynamic measurements on a
1065 4.5 m diameter rotor placed in the large German Dutch Wind Tunnel DNW, *Journal of Physics: Conference Series*, 555, 012 089, <https://doi.org/10.1088/1742-6596/555/1/012089>, 2014.
- Schreiber, J., Nanos, E. M., Campagnolo, F., and Bottasso, C. L.: Verification and calibration of a reduced order wind farm model by wind tunnel experiments, in: *Journal of Physics: Conference Series*, vol. 854, p. 012041, IOP Publishing, <https://doi.org/10.1088/1742-6596/854/1/012041>, 2017.
- Schreiber, J., Balbaa, A., and Bottasso, C. L.: Brief communication: A double-Gaussian wake model, *Wind Energy Science*, 5, 237–244,
1070 <https://doi.org/10.5194/wes-5-237-2020>, 2020a.
- Schreiber, J., Bottasso, C. L., and Bertelè, M.: Field testing of a local wind inflow estimator and wake detector, *Wind Energy Science*, 5, 867–884, <https://doi.org/10.5194/wes-5-867-2020>, 2020b.
- Schreiber, J., Bottasso, C. L., Salbert, B., and Campagnolo, F.: Improving wind farm flow models by learning from operational data, *Wind Energy Science*, 5, 647–673, <https://doi.org/10.5194/wes-5-647-2020>, 2020c.
- 1075 Sengers, B. A. M., Steinfeld, G., Hulsman, P., and Kühn, M.: Validation of an interpretable data-driven wake model using lidar measurements from a free-field wake steering experiment, *Wind Energy Science*, 8, 747–770, <https://doi.org/10.5194/wes-8-747-2023>, 2023.
- Sharma, A., Brazell, M. J., Vijayakumar, G., Ananthan, S., Cheung, L., deVelder, N., Henry de Frahan, M. T., Matula, N., Mullaney, P., Rood, J., Sakievich, P., Almgren, A., Crozier, P. S., and Sprague, M.: ExaWind: Open-source CFD for hybrid-RANS/LES geometry-resolved wind turbine simulations in atmospheric flows, *Wind Energy*, 27, 225–257, <https://doi.org/10.1002/we.2886>, 2024.
- 1080 Shaukat, U. and Giljarhus, K. E. T.: Precursor turbulent inflow dataset for large eddy simulation of a semi-idealized European generic city, *Data in Brief*, 54, 110467, <https://doi.org/10.1016/j.dib.2024.110467>, 2024.
- Smith, M. J., Lim, J. W., van der Wall, B. G., Baeder, J. D., Biedron, R. T., Boyd Jr, D. D., Jayaraman, B., Jung, S. N., and Min, B.-Y.: The HART II international workshop: an assessment of the state of the art in CFD/CSD prediction, *CEAS Aeronautical Journal*, 4, 345–372, <https://doi.org/10.1007/s13272-013-0078-8>, 2013.



- 1085 Snel, H., Schepers, J. G., and Montgomerie, B.: The MEXICO project (Model Experiments in Controlled Conditions): The database and first results, *Journal of Physics: Conference Series*, 75, 012 014, <https://doi.org/10.1088/1742-6596/75/1/012014>, 2007.
- Styrk Andersen, M., Isaksen, B., and Hansen, S. O.: Full-scale monitoring of the wind field, surface pressures and structural response of Gjemnessund suspension bridge, *Structural Engineering International*, 32, 43–54, <https://doi.org/10.1080/10168664.2021.1953426>, 2022.
- Tamaro, S., Campagnolo, F., and Bottasso, C. L.: On the power and control of a misaligned rotor–beyond the cosine law, *Wind Energy Science*, 9, 1547–1575, <https://doi.org/10.5194/wes-9-1547-2024>, 2024.
- 1090 Tamaro, S., Bortolin, D., Campagnolo, F., Mühle, F. V., and Bottasso, C. L.: Scaled testing of maximum-reserve active power control, Zenodo [source code and data set], <https://doi.org/10.5281/zenodo.17551525>, 2025.
- Tamaro, S., Bortolin, D., Campagnolo, F., Mühle, F. V., and Bottasso, C. L.: Scaled testing of maximum-reserve active power control, *Wind Energy Science*, 11, 1607–1630, <https://doi.org/10.5194/wes-11-1607-2026>, 2026.
- 1095 The MathWorks Inc.: MATLAB version: 9.14.0 (R2023a), <https://www.mathworks.com>, last accessed: 2025-12-12, 2023.
- Tinoco, E.: Summary data from the seventh AIAA CFD drag prediction workshop, in: *AIAA Aviation 2023 Forum*, p. 3492, <https://doi.org/10.2514/6.2023-3492>, 2023.
- Tinoco, E. N., Brodersen, O. P., Keye, S., Laffin, K. R., Feltrop, E., Vassberg, J. C., Mani, M., Rider, B., Wahls, R. A., Morrison, J. H., et al.: Summary data from the sixth AIAA CFD drag prediction workshop: CRM cases, *Journal of Aircraft*, 55, 1352–1379, <https://doi.org/10.2514/1.C034409>, 2018.
- 1100 Tominaga, Y. and Shirzadi, M.: Wind tunnel measurement dataset of 3D turbulent flow around a group of generic buildings with and without a high-rise building, *Data in Brief*, 39, 107 504, <https://doi.org/10.1016/j.dib.2021.107504>, 2021.
- van der Wall, B. G.: A comprehensive rotary-wing data base for code validation: the HART II international workshop, *Aeronautical Journal*, 115, 91, <https://doi.org/10.1017/S0001924000005480>, 2011.
- 1105 van der Wall, B. G., Burley, C. L., Yu, Y., Richard, H., Pengel, K., and Beaumier, P.: The HART II test–measurement of helicopter rotor wakes, *Aerospace Science and Technology*, 8, 273–284, <https://doi.org/10.1016/j.ast.2004.01.001>, 2004.
- van Dooren, M. F., Kühn, M., Petrović, V., Bottasso, C. L., Campagnolo, F., Sjöholm, M., Angelou, N., Mikkelsen, T., Croce, A., and Zasso, A.: Demonstration of synchronised scanning lidar measurements of 2d velocity fields in a boundary-layer wind tunnel, in: *Journal of Physics: Conference Series*, vol. 753, p. 072032, IOP Publishing, <https://doi.org/10.1088/1742-6596/753/7/072032>, 2016.
- 1110 van Dooren, M. F., Campagnolo, F., Sjöholm, M., Angelou, N., Mikkelsen, T., and Kühn, M.: Demonstration and uncertainty analysis of synchronised scanning lidar measurements of 2-D velocity fields in a boundary-layer wind tunnel, *Wind Energy Science*, 2, 329–341, <https://doi.org/10.5194/wes-2-329-2017>, 2017.
- Veers, P., Bottasso, C. L., Manuel, L., Naughton, J., Pao, L., Paquette, J., Robertson, A., Robinson, M., Ananthan, S., Barlas, T., et al.: Grand challenges in the design, manufacture, and operation of future wind turbine systems, *Wind Energy Science*, 8, 1071–1131, <https://doi.org/10.5194/wes-8-1071-2023>, 2023.
- 1115 Wang, C., Wang, J., Campagnolo, F., Carraón, D. B., and Bottasso, C. L.: Validation of large-eddy simulation of scaled waked wind turbines in different yaw misalignment conditions, in: *Journal of Physics: Conference Series*, vol. 1037, p. 062007, IOP Publishing, <https://doi.org/10.1088/1742-6596/1037/6/062007>, 2018a.
- Wang, C., Campagnolo, F., and Bottasso, C. L.: Does the use of load-reducing IPC on a wake-steering turbine affect wake behavior?, in: *Journal of Physics: Conference Series*, vol. 1618, p. 022035, IOP Publishing, <https://doi.org/10.1088/1742-6596/1618/2/022035>, 2020a.
- 1120 Wang, C., Campagnolo, F., and Bottasso, C. L.: Identification of airfoil polars from uncertain experimental measurements, *Wind Energy Science*, 5, 1537–1550, <https://doi.org/10.5194/wes-5-1537-2020>, 2020b.



- 1125 Wang, C., Campagnolo, F., Sharma, A., and Bottasso, C. L.: Effects of dynamic induction control on power and loads, by LES-ALM simulations and wind tunnel experiments, in: *Journal of Physics: Conference Series*, vol. 1618, p. 022036, IOP Publishing, <https://doi.org/10.1088/1742-6596/1618/2/022036>, 2020c.
- Wang, C., Muñoz-Simon, A., Deskos, G., Laizet, S., Palacios, R., Campagnolo, F., and Bottasso, C. L.: Code-to-code-to-experiment validation of LES-ALM wind farm simulators, in: *Journal of Physics: Conference Series*, vol. 1618, p. 062041, IOP Publishing, <https://doi.org/10.1088/1742-6596/1618/6/062041>, 2020d.
- 1130 Wang, C., Campagnolo, F., Canet, H., Barreiro, D. J., and Bottasso, C. L.: How realistic are the wakes of scaled wind turbine models?, *Wind Energy Science*, 6, 961–981, <https://doi.org/10.5194/wes-6-961-2021>, 2021.
- Wang, J., Foley, S., Nanos, E. M., Yu, T., Campagnolo, F., Bottasso, C. L., Zanotti, A., and Croce, A.: Numerical and experimental study of wake redirection techniques in a boundary layer wind tunnel, in: *Journal of Physics: Conference Series*, vol. 854, p. 012048, IOP Publishing, <https://doi.org/10.1088/1742-6596/854/1/012048>, 2017a.
- 1135 Wang, J., Mclean, D., Campagnolo, F., Yu, T., and Bottasso, C. L.: Large-eddy simulation of waked turbines in a scaled wind farm facility, in: *Journal of Physics: Conference Series*, vol. 854, p. 012047, IOP Publishing, <https://doi.org/10.1088/1742-6596/854/1/012047>, 2017b.
- Wang, J., Wang, C., Castañeda, O. D., Campagnolo, F., and Bottasso, C. L.: Large-eddy simulation of scaled floating wind turbines in a boundary layer wind tunnel, in: *Journal of Physics: Conference Series*, vol. 1037, p. 072032, IOP Publishing, <https://doi.org/10.1088/1742-6596/1037/7/072032>, 2018b.
- 1140 Wang, J., Wang, C., Campagnolo, F., and Bottasso, C. L.: Wake behavior and control: comparison of LES simulations and wind tunnel measurements, *Wind Energy Science*, 4, 71–88, <https://doi.org/10.5194/wes-4-71-2019>, 2019.
- Zengler, C. P., Braunbehrens, R., and Tamaro, S.: Further improvements to the double-Gaussian wake model, in: *Journal of Physics: Conference Series*, vol. 2767, p. 092066, IOP Publishing, <https://doi.org/10.1088/1742-6596/2767/9/092066>, 2024.